GL01248

IDO/ DOE/ET27002-4

INTEGRAL EQUATION MODELING OF THREE-DIMENSIONAL MAGNETOTELLURIC RESPONSE

By

S. C. TING and G. W. HOHMANN

Work performed under Contract No.

DE-AC07-79ET/27002

Department of Geology and Geophysics

University of Utah

Salt Lake City, Utah (USA)

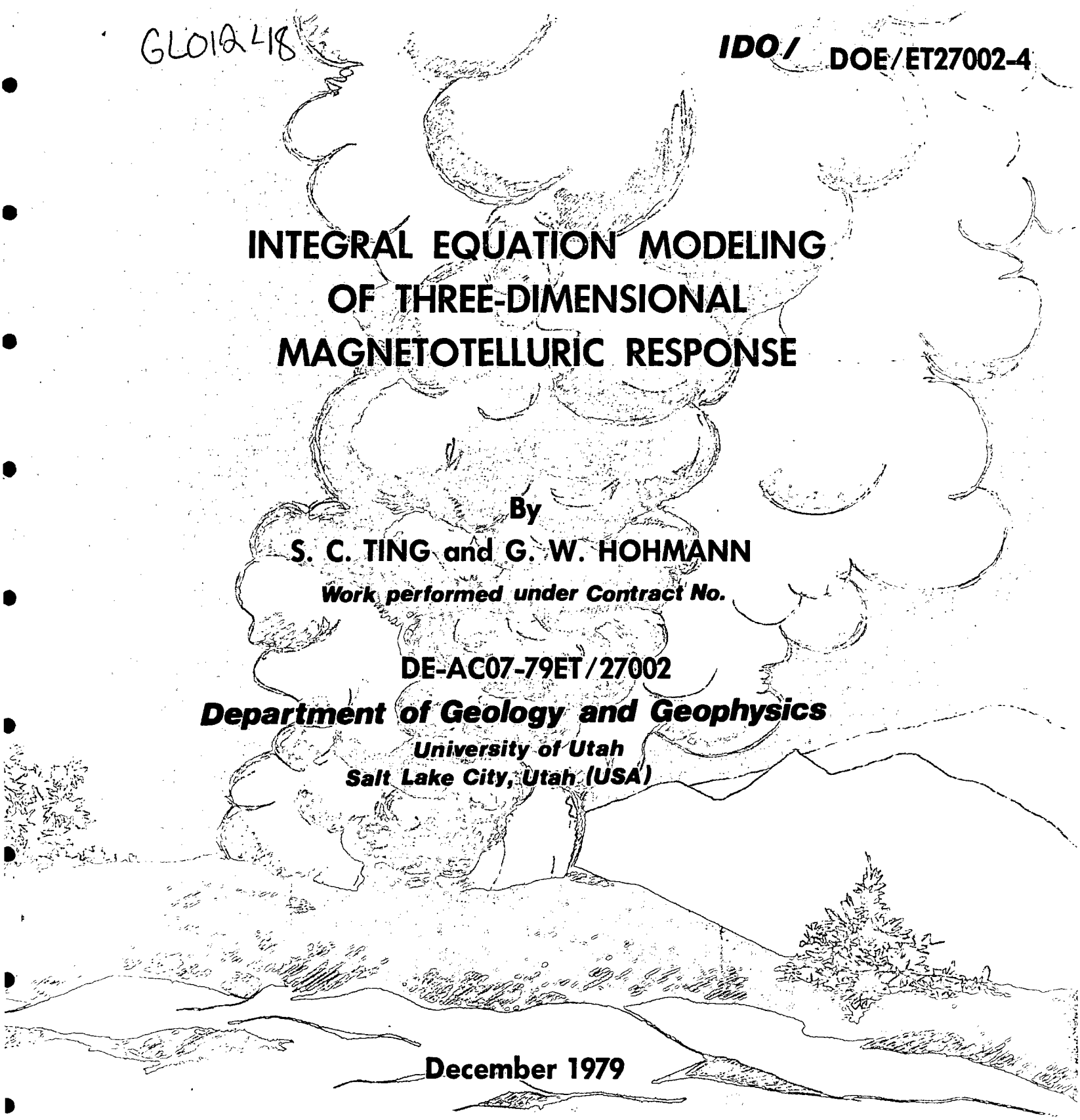

December 1979

Prepared for

DEPARTMENT OF ENERGY

Division of Geothermal Energy

NOTICE

This report was prepared to document work sponsored by the United States Government. Neither the United States nor its agent, the United States Department of Energy, nor any Federal employees, nor any of their contractors, subcontractors or their employees, makes any warranty, express or implied, or assumes any legal liability or responsibility for the accuracy, completeness, or usefulness of any information, apparatus, product or process disclosed, or represents that its use would not infringe privately owned rights.

NOTICE

Reference to a company or product name does not imply approval or recommendation of the product by the University of Utah or the U.S. Department of Energy to the exclusion of others that may be suitable.

INTEGRAL EQUATION MODELING OF THREE-DIMENSIONAL MAGNETOTELLURIC RESPONSE

BY

Sam C. Ting* and Gerald W. Hohmann*

Presented at the 48th Annual International SEG Meeting, November 1, 1978, San Francisco, California

*Department of Geology and Geophysics, University of Utah
Salt Lake City, Utah 84112

ABSTRACT

We have adapted a three-dimensinal (3D) volume integral equation to magnetotelluric (MT) modeling. Incorporating an integro-difference scheme increases the accuracy somewhat. Utilizing the two symmetry planes of a buried prismatic body and a normally incident plane wave source greatly reduces the required computation time and storage. Convergence checks and comparisons with one-dimensional (1D) and two-dimensional (2D) models indicate that our results are valid.

In this paper, we show theoretical surface anomalies due to a 3D prismatic conductive body buried in a half-space earth. Instead of studying the electric and magnetic fields, we have obtained impedance tensor and magnetic transfer functions by imposing two different source polarizations. Manipulation of the impedance tensor and magnetic transfer functions yields the following MT quantities: apparent resistivity and phase, impedance polar diagrams, tipper direction and magnitude, principal directions, skew and ellipticity. With our preliminary analyses of these MT quantities, we have found that three-dimensionality is usually revealed by all of them. Furthermore, we have recognized two pairs of complementary parameters; apparent resistivity and phase, and skew and ellipticity. Because of surface charges at conductivity boundaries, low-frequency 3D responses are much different from 1D and 2D responses. Thus, in many cases 3D models are required for interpreting MT data.

Although an overall 3D MT interpretation is still not practical, combined 2D and 3D modeling could be applied to yield a

gross 3D structure, which is composed of a cross section and its strike extent. In doing so, we suggest that the cross section be obtained from higher frequency 2D $E_{\perp}$ mode modeling, and that the strike extent be derived by matching with lower frequency $E_{\parallel}$ mode results due to corresponding 3D models. In addition, we have indicated that some simple 3D features, e.g., location above conductive zone, corners, and symmetry lines, can be easily recognized.

INTRODUCTION

The magnetotelluric (MT) method, which makes use of naturally occuring electromagnetic fields is one of the most widely used electrical prospecting techniques due to its potential for deep exploration. However, MT has been hampered severly by a lack of interpretational capability. Inappropriate one-dimensional (1D) and two-dimensional (2D) interpretation models are often used because the necessary three-dimensional (3D) models are not readily available. These simple interpretation algorithms are useful in some geological situations where 1D or 2D models apply. However, the results can be quite misleading in cases where the earth is three-dimensional and the 'E' parallel ($E_{\parallel}$) and 'E' perpendicular ($E_{\perp}$) modes do not separate.

There are two basic approaches to numerical modeling: (1) differential equation (DE) and (2) integral equation (IE) methods. Both methods are useful and necessary. Differential equation solutions are easier to set up, and they result in large banded matrices. Because the entire earth is modeled on a grid, DE methods are preferable for modeling complex geology. Integral equation formulations involve more difficult mathematics, but their advantage is that unknown fields need be found only in anomalous regions. Thus, integral equation solutions are less expensive for simulating the response of one or a few small bodies and hence more useful for evaluating field techniques, for designing surveys, and for generating catalogs of interpretation curves.

We have refined and adapted an integral equation solution

(Hohmann, 1975) so that it can be used to simulate the MT response of a 3D body in a half space (Hohmann and Ting, 1978). MT modeling is easier than our previous controlled-source EM modeling because of the lower frequencies, lower conductivities and deeper targets, and smoother fields. Furthermore, for bodies which have vertical symmetry planes, both the computer time and storage are greatly reduced, which makes 3D modeling economically feasible.

In the past few years, 3D geophysical EM solutions have been given by others (Jones, 1974; Weidelt, 1975; Reddy et al., 1977; Jones and Vozoff, 1978). However, all of those results have been presented without adequate crosschecks. In addition, the accuracy of results obtained from any numerical method will be affected by the discretization of the work domain, and little attention has been paid to this matter in the published work.

In this paper, we have done our best to address the two problems mentioned above. The validity of our solution is supported by a convergence check and comparison with 1D and 2D models. Although we are not able to give quantitatively the accuracy of our 3D solution, all the 3D models in this paper have been discretized fine enough to yield reasonably accurate results based on the convergence check.

For readers who are not familiar with the integral equation theory, we have given a brief review of the theory at the outset. The details are given in Hohmann (1975) and Hohmann and Ting (1978). In the remainder of the paper, various MT functions over a 3D prismatic body buried in a half-space earth are analyzed.

THEORY

Consider the configuration shown in Figure 1, the earth is taken to be a half-space of conductivity σ_1, except for a rectangular inhomogeneity having variable conductivity $\sigma_2(\bar{r})$. Since a plane wave normally incident upon the earth is usually assumed for MT sounding we begin with the source-free Maxwell's equations (in mks units) in the frequency domain ($e^{i\omega t}$ time dependence):

$$\nabla \times \bar{E} + i\omega\mu_0 \bar{H} = 0 \tag{1}$$

$$\nabla \times \bar{H} - \sigma \bar{E} = 0 \tag{2}$$

where we have assumed that the magnetic permeability in the earth is the same as it is in free space and where we have neglected displacement currents in the earth.

We define the primary fields as the homogeneous-earth fields described by

$$\nabla \times \bar{E}^p + i\omega\mu_0 \bar{H}^p = 0 \quad , \tag{3}$$

and

$$\nabla \times \bar{H}^p - \sigma_1 \bar{E}^p = 0 \quad . \tag{4}$$

Substracting (3) from (1) and (4) from (2) yields

$$\nabla \times (\bar{E} - \bar{E}^p) + i\omega\mu_0 (\bar{H} - \bar{H}^p) = 0 \quad , \tag{5}$$

$$\nabla \times (\bar{H} - \bar{H}^p) - \sigma \bar{E} + \sigma_1 \bar{E}^p = 0 \quad . \tag{6}$$

Note that σ is the actual value of conductivity anywhere below the surface: it is equal to $\sigma_2(\bar{r})$ in the inhomogeneity and σ_1 elsewhere in the earth.

Now we rewrite (6) as

$$\nabla \times (\bar{H} - \bar{H}^p) - \sigma_1(\bar{E} - \bar{E}^p) + (\sigma_1 - \sigma)\,\bar{E} = 0 \quad . \tag{7}$$

If the difference fields are treated as secondary fields and denoted by superscript 's', (5) and (7) become:

$$\nabla \times \bar{E}^s + i\omega\mu_0 \bar{H}^s = 0 \quad , \tag{8}$$

and

$$\nabla \times \bar{H}^s - \sigma_1 \bar{E}^s = \bar{J}^s \quad , \tag{9}$$

where

$$\bar{J}^s = [\sigma_2(\bar{r}) - \sigma_1]\,\bar{E} \tag{10}$$

is the polarization or scattering current which exists only in the inhomogeneity.

Hence the electromagnetic field has been split into two components, denoted as primary and secondary fields. The primary field is the field that would be present if the earth were homogeneous. It can be obtained easily by solving (3) and (4). The secondary field is due to the polarization current in the inhomogeneity. It can be found by treating $\bar{J}^s$ as a source current, converting (8) and (9) to an integral equation, and solving

numerically. The secondary electric field is given by

$$\bar{E}^s = -i\omega\mu_0\bar{A} - \nabla\phi \quad , \tag{11}$$

where $\bar{A}$ and ϕ are vector and scalar potentials (Harrington, 1968), given in the earth by

$$\bar{A}\,(\bar{r}) = \int_v \bar{J}^s(\bar{r}')\; G\;(\bar{r},\, \bar{r}')\; dv' \quad , \tag{12}$$

and

$$\phi(\bar{r}) = -\frac{1}{\sigma_1}\int_v \nabla' \cdot \bar{J}^s\;(\bar{r}')\; G\;(\bar{r},\, \bar{r}')\; dv' \quad , \tag{13}$$

where G is a scalar Green's function, which for a whole space is given by

$$G\;(\bar{r},\, \bar{r}') = \frac{e^{-ik_1\,|\bar{r} - \bar{r}'|}}{4\pi\,|\bar{r} - \bar{r}'|} \quad . \tag{14}$$

For a body in a half space, additional terms must be added to the potentials to account for image currents in the air. The secondary field is due to currents and charges, as defined by (11), (12), and (13). The charges occur at discontinuities in $\bar{J}^s$, both inside the body (due to the discretization scheme) and at the boundaries of the body.

Adding the incident and secondary fields, we obtain an integral equation

$$\bar{E} = \bar{E}^p - i\omega\mu_0\bar{A} - \nabla\phi \quad , \tag{15}$$

which can be written symbolically as

$$\bar{E}(\bar{r}) = \bar{E}^p(\bar{r}) + \int_V [\sigma_2(\bar{r}') - \sigma_1]\, \bar{\bar{G}}(\bar{r}, \bar{r}') \cdot \bar{E}(\bar{r}')\, dv' \quad , \quad (16)$$

where $\bar{\bar{G}}$ is the half-space dyadic Green's function (Tai, 1971) which accounts for the earth-air interface.

For a numerical solution, Hohmann (1975), Weidelt (1975), and Meyer (1976) divided the inhomogeneity into N cubic cells as shown in Figure 2, and used pulse subsectional basis functions (Harrington, 1968) to represent the unknown electric field in the inhomogeneity. Conductivity is taken to be constant in each cell. This amounts to assuming that the polarization current is constant throughout each cell. The integration over the dyadic Green's function in (16) can be carried out numerically (Meyer, 1976) or analytically over the volumes and surfaces of the cells (Hohmann, 1975) to obtain the equation

$$\bar{E}(\bar{r}) = \bar{E}^p(\bar{r}) + \sum_{n=1}^{N} (\sigma_{2_n} - \sigma_1)\, \bar{\bar{\Gamma}}(\bar{r}, \bar{r}') \cdot \bar{E}_n \quad , \quad (17)$$

where $\bar{E}_n$ is the electric field and σ_{2n} is the conductivity in cell n. $\bar{\bar{\Gamma}}$ is the dyadic Green's function for a finite cube of current, unlike $\bar{\bar{G}}$ which applies to an infinitesimal current element. Care must be taken in deriving $\bar{\bar{\Gamma}}$, because $\bar{\bar{G}}$ is singular at $\bar{r} = \bar{r}'$.

We have derived (17) in a manner similar to that described by Hohmann (1975), except that, following Harrington (1968), we approximate the derivatives of the scalar potential in (11) with differences. Also instead of concentrating the charge (the $\nabla \cdot \bar{J}^s$ term in (13)) at the boundaries between cells, we distribute it uniformly over a volume extending from the center of one cell to the center of the next cell (Hohmann and Ting, 1978).

As various authors have indicated, approximating derivatives with differences provides accuracy similar to that of smooth basis functions but is much easier to implement on a computer. See, e.g., Miller and Deadrick (1974), and Butler and Wilton (1975).

In more concise notation, the electric field at the center of cell m is given by writing (17) in the form

$$\bar{E}_m = \bar{E}_m^p + \sum_{n=1}^{N} (\sigma_{2_n} - \sigma_1)\, \bar{\bar{\Gamma}}_{mn} \cdot \bar{E}_n \quad . \tag{18}$$

Rearranging (18), we get

$$\sum_{n=1}^{N} [(\sigma_{2_n} - \sigma_1)\, \bar{\bar{\Gamma}}_{mn} - \bar{\bar{\delta}}_{mn}] \cdot \bar{E}_n = -\bar{E}_m^p \tag{19}$$

in which

$$\bar{\bar{\delta}}_{mn} = \begin{cases} \bar{\bar{I}} , & m = n \\ \bar{\bar{0}} , & m \neq n \end{cases} , \tag{20}$$

where $\bar{\bar{I}}$ is the 3 x 3 unit dyadic and $\bar{\bar{0}}$ is the 3 x 3 null dyadic.

Writing (19) for each of the N values of m produces a partitioned matrix equation

$$[\bar{\bar{M}}] \cdot [\bar{E}] = -[\bar{E}^p] \tag{21}$$

to solve for the electric field in the cells. The elements of the matrix are themselves 3 x 3 matrices, given by

$$M_{mn} = (\sigma_{2_n} - \sigma_1)\, \bar{\bar{\Gamma}}_{mn} - \bar{\bar{\delta}}_{mn} \quad . \tag{22}$$

Once (21) is solved for the fields in the cells, the electric field at any point outside the inhomogeneity can be calculated from

(17), while the magnetic field can be obtained easily by applying equation (1) to (17).

SIMPLIFICATIONS FOR SYMMETRIC BODIES

The MT source is assumed to produce normally incident plane waves in the earth. If the inhomogeneity has any vertical symmetry planes, the total fields in the inhomogeneity must be either symmetric or antisymmetric. To solve the final matrix equation, we only need to examine part of the inhomogeneous body.

For the simple models which we consider in this paper, there are two vertical planes of symmetry passing through the center of the body. Hence it is only necessary to solve for one-fourth of the total number of unknowns in any quadrant.

Unfortunately the resulting matrix, for a problem with symmetry planes, is not symmetric as it is in the general case, for equal-conductivity and equal-size cells. Even so, the computer storage and computation time are reduced considerably. In the general case $3N(3N + 1)/2 \approx 9N^2/2$ storage locations are required, where N is the number of cells. With two symmetry planes, the storage requirement is $(3N/4) \times (3N/4) = 9N^2/16$ -- less by a factor of 8. Furthermore, the conductivities and sizes of the cells can be different. Figure 3 illustrates the comparison in computer time. In each case, forming and factoring (LU decomposition) the matrix account for most of the computer time. Matrix factorization time is less by a factor of about 35 when symmetry is invoked. The time required to form the matrix is less for the symmetric problem, because only one-fourth of the matrix elements need to be computed.

In the general case a maximum of 120 cells can be used on the

University of Utah Univac 1108 computer, but for a prismatic body with two vertical symmetry planes the limitation is 340 cells. This increase in the number of cells as well as the flexibility of choosing cells with different sizes and conductivities permit us to model large or shallow bodies more accurately or, alternatively, to model several bodies.

CHECKS ON THE SOLUTION

Because of the many possibilities for theoretical and programming errors, it is important to verify the accuracy of any numerical solution. The best check is with results from another type of numerical solution. Unfortunately, the only other published 3D MT results are those of Jones (1974), Weidelt (1975), and Reddy et al., (1977), all for outcropping bodies which we cannot model accurately. However, convergence checks as well as comparisons with 1D and 2D models, which are shown in the following sections, lend credence to our results.

Convergence Check

An important self-check is convergence: as the discretization is made finer, the results should converge to some value. The model we have used to check convergence is a 1 km x 2 km x 2 km conductive prism buried in a 100 Ω-m earth. To see how the resistivity and depth of the prism affect our results, we have chosen four cases, by using two prism resistivities, 0.5 Ω-m and 5 Ω-m, and two depths, 250 m and 500 m. Three discretizations used for the prism are shown in Figure 4. The hybrid discretization in the middle is a transition between the top and bottom discretization. We have checked convergence at the earth's surface above the center and above the lower left corner of the prism as shown in Figures 5 and 6 respectively. Since all apparent resistivities and phase angles derived from the impedance tensor have about the same convergence, we have only shown results of one apparent resistivity, ρ_{xy}.

It is clear that our results are converging. In Figures 5a and 5b, we see that the convergence improves drastically as the resistivity of the prism increases by a factor of 10. Furthermore, convergence tends to become worse as the frequency increases, except at the highest frequency where the response due to the prism is dying out. The above phenomena can be explained partly by the concept of skin depth. As we decrease the resistivity in the prism or increase the frequency, the skin depth in the prism becomes less which means that fields are varying more rapidly. Conductivity contrast also affects the variation of fields within the prism. Because we have assumed the electric field is constant within each cell, more rapid field variation requires smaller cells. Smooth basis functions would be more desirable than our pulse functions, but they are very difficult to implement in three dimensions.

Another factor which affects convergence is the depth of the prism. When the prism is made shallower, from 500 m to 250 m, convergence gets worse, as shown in Figure 5. The poor convergence at this shallow depth is mainly attributed to the inaccuracy of the constant-cell approximation when the observation point is too close to the cells and when the secondary fields are greater. On the other hand, we have obtained results (not shown here) for the prism buried at a greater depth, 1000 m, and have noticed that, at both conductivity contrasts and at all the frequencies, results for all the discretizations lie within 5% of each other. The essence of above observation is to tell us to use smaller cells in the shallow part, and larger cells in the deeper part of the prism. As we can see, the

results of a hybrid discretization, which is the middle case in Figure 4, are close to those of the finest discretization. However, the ratio of computation cost for these two cases is about 1 to 10.

Figure 6 shows results above the lower left corner of the prism. Because the secondary fields here are much weaker compared to those over the center of the prism, convergence is satisfactory for all the cases because the major contribution is coming from the primary fields.

From the above discussion, we note that the convergence of our results depends on many factors: cell size, conductivity within and surrounding the inhomogeneity, frequency, depth of burial, all of which are coupled together. Because convergence is affected by so many factors, we are not able to quantify accurately any general criteria among those factors to assure a certain accuracy in our results.

Comparison with One-dimensional Model

To examine the validity of 1D interpretation over a 3D body, we compared theoretical results for a three layer model with those for horizontal 3D square slabs in place of the middle layer. The 1D model consists of an anomalous layer with resistivity 5 Ω-m and thickness 100 m buried 200 m deep in a half space of resistivity 100 Ω-m. To compare with 3D models, we replace the infinite anomalous layer by a finite square slab having different lateral extents. The apparent resistivity is calculated over the center of the slabs and plotted as a function of frequency. The comparison is shown in Figure 7 for

square slabs 400, 800, 1200 and 1600 meters on a side. All the slabs are discretized into 100 m cubes. We believe the 3D results should be reasonably accurate based on the convergence check.

Due to the storage limitation on our computer, the largest slab we can run is 1600 m by 1600 m. Our 3D results appear to be converging to the 1D curve, but the convergence is very slow at the lower frequencies. This illustrates the important point that because of surface charges at its boundaries are important, a 3D slab must be very large for 1D interpretation to apply. If 1D inversion is applied to the results obtained for our largest slab, the results will be erroneous.

Comparison with Two-dimensional Model

Another useful check, and one which is enlightening for MT interpretation, is the comparison between results for elongated 3D prisms and those for a 2D model with the same cross section. In the three-dimensional case the currents are not confined to flow parallel as in the two-dimensional (TE) case, but may be deflected laterally by regions of different conductivity. This lateral flow of current affects the nature of the fields near structures of finite extent in all three dimensions, and these effects are reflected in the theoretically calculated apparent resistivity values. With this in mind, it is useful to compare apparent resistivity curves to obtain some indication of the effect the finite extent of the three-dimensional structure makes in the calculations.

Figures 8 and 9 show comparisons between our 3D results and 2D

results computed with Rijo's (1977) finite element algorithm at 0.1 Hz and 10 Hz. Three different strike extents are shown in the figures. Discretization in the cross section of the 3D prisms is the same as the hybrid case in Figure 4. Since we are only interested in the center profile, larger cells (500 m cubes) were used near the long ends of the prism which not only saves significant computer time but also allows us to run a 12-km-long prism. Discretization of the 3D prisms has been carefully designed and checked on the basis of our convergence check to assure all the results are reasonably accurate.

Figure 8 shows the comparison for the incident electric field parallel to the strike direction ($E_{\parallel}$ mode). Apparent resistivity is plotted along a profile across the center of the prism. The secondary electric field due to surface charges at the ends of the body becomes important at lower frequencies while that due to volume currents decreases with decreasing frequency. 3D results approach the 2D curve at the lower frequency as the length increases, but significant difference still exists between the longest prism and the 2D model. This is primarily due to the surface charges which accumulate at the boundaries perpendicular to current flow in the 3D prism, which do not appear in the 2D case. At 10 Hz all the results are very close to those of the 2D model because surface charges do not have a significant role compared to volume currents and the contribution from the far ends of the prism has been severely attenuated.

Letting the incident electric field be perpendicular to strike ($E_{\perp}$ mode) we obtain another comparison, shown in Figure 9. Surface charges are included implicitly in the 2D $E_{\perp}$ formulation, and two

solutions do not diverge as much as they do for the $E_{\parallel}$ mode at the low frequency. Near the center of the profile, note that our results are converging, but not toward the 2D curve. The possible reason could be: (1) our longest prism is still not long enough to resemble the 2D model, (unfortunately, we are not able to make the prism any longer with the limited storage in our computer), or (2) error introduced by our constant-cell approximation, or (3) error in the 2D results. We think the most probable reason is (2).

By looking at the 2D-3D comparison in Figures 8 and 9, we notice that, at least for our simple prismatic model, 2D $E_{\perp}$ modeling could be applied to the 3D $E_{\perp}$ mode results to reveal the earth cross section at the center profile (Wannamaker, 1979). Low frequency 3D $E_{\parallel}$ mode results are much different from their corresponding 2D results. Therefore, 2D $E_{\parallel}$ mode interpretation can be misleading if the data are three dimensional. On the other hand, since 3D $E_{\parallel}$ mode results at the lower frequency are very sensitive to the strike extent, it should not be difficult to resolve the strike extent of a gross three dimensional structure by studying its low frequency $E_{\parallel}$ mode data if we assume that its cross section does not vary along the strike. In doing so, we suggest that the cross section be obtained from higher frequency 2D $E_{\perp}$ mode modeling, and that the strike extent be derived by matching with lower frequency $E_{\parallel}$ mode results due to corresponding 3D models.

One important question is: How long must an elongated 3D prism be for its response to resemble a 2D structure? From Figures 8 and 9, we notice that the answer to the above question not only depends on the mode ($E_{\parallel}$ or $E_{\perp}$), but also is heavily influenced by the frequency.

The comparisons in Figures 8 and 9 are useful for two reasons: (1) they support the validity of the 3D solution, and (2) they point out the problems in interpreting data with 2D models. Because there are lateral conductivity boundaries in all directions for a typical three-dimensional application of MT, all fields are interrelated and can not be separated. As deduced by Wannamaker (1978), standard mode identification is invalid, and 3D models are required for interpretation.

PRESENTATION OF VARIOUS MT PARAMETERS FOR A SIMPLE 3D EARTH MODEL

In MT work, we usually do not interpret the electric and magnetic fields themselves because they depend on the source fields, over which we have no control. Instead, we look at the relationships between these fields, such as impedance tensor and magnetic transfer functions. They all contain information about the subsurface; however, it is very difficult to make any physical interpretation by looking directly at them. Therefore, some manipulation of these two quantities is necessary to yield more recognizable parameters.

In this section, we show surface contour maps of various MT parameters due to a 3D prism buried in a half-space earth, which is shown in Figure 10. The prism is discretized into 250 m cubes which should make the results very accurate. Because there are two vertical symmetry planes, results are shown for the lower right quadrant only. For the benefit of others who might want to compare with our results, we have included numerical data at some selected points on all the contour diagrams.

Apparent Resistivity and Phase Along Original Coordinate System

The horizontal magnetic and electric fields at the earth's surface can be related by the frequency domain expression

$$E_x = Z_{xx}H_x + Z_{xy}H_y \quad , \quad (23)$$

and

$$E_y = Z_{yx}H_x + Z_{yy}H_y \quad , \quad (24)$$

or in a concise form

$$\{\bar{E}\} = \{\bar{\bar{Z}}\} \{\bar{H}\} \quad , \quad (25)$$

where $$\bar{\bar{Z}} = \begin{bmatrix} Z_{xx} & Z_{xy} \\ Z_{yx} & Z_{yy} \end{bmatrix} \quad . \quad (26)$$

$\bar{E}$ and $\bar{H}$ are vectors formed by (E_x, E_y) and (H_x, H_y) respectively, and $\bar{\bar{Z}}$ is the impedance tensor. To solve for the four unknowns in $\bar{\bar{Z}}$, we have to impose another source polarization to obtain two more equations

$$E_{x_2} = Z_{xx}H_{x_2} + Z_{xy}H_{y_2} \quad (27)$$

$$E_{y_2} = Z_{yx}H_{x_2} + Z_{yy}H_{y_2} \quad (28)$$

where we have used subscript '2' to designate fields generated by the second source polarization. This second set of fields can be easily obtained by changing only the right hand side of equation (21).

The impedance tensor obtained through the above equations (23), (24), (27), and (28), is transformed to apparent resistivity and phase by the following simple formulae

$$\rho_{ij} = |Z_{ij}|^2/\mu_o\omega \quad (29)$$

$$\theta_{ij} = \tan^{-1} [I_m(Z_{ij})/Re(Z_{ij})] \qquad i,j = x,y \quad , \quad (30)$$

where $Im(Z_{ij})$ and $Re(Z_{ij})$ are the imaginary and real parts of Z_{ij} respectively, and where the phase θ_{ij} is the angle measured counter-clockwise in the complex plane. Because the impedance tensor varies with respect to the coordinate system, apparent resistivity and phase derived from it also vary with the coordinate system.

Figures 11 and 12 show surface contours of the apparent resistivity along the original coordinate system at 0.1 Hz and 10 Hz respectively. On the coordinate axes, on-diagonal apparent resistivities, ρ_{xx} and ρ_{yy} are zero, which means the fields could be decomposed into the E and E mode as in the 2D case. This happens as a coincidence because our coordinate system is right on the symmetry lines of the earth model. Near the corner, ρ_{xx} and ρ_{yy} approach their maximum which is purely due to the three dimensionality. Because three dimensionality is more important at the lower frequency, ρ_{xx} and ρ_{yy} are much greater at 0.1 Hz than they are at 10 Hz. Also because of the symmetry of the model, contours of ρ_{xy} and ρ_{yx} have a similar pattern except for a 90-degree rotation.

The corresponding phase contours are shown in Figures 13 and 14. xx and yy are neglected on the coordinate axes where the on-diagonal impedance elements, Z_{xx} and Z_{yy} are near-zero unstable numbers. Unlike apparent resistivity, phase contours do not explicitly show the three dimensionality. Furthermore, we see stronger variation, which means higher resolving power, of phase at the higher frequency in contrast to the small variation diagnostic of apparent resistivity at the higher frequency. This suggests that apparent resistivity and phase are really two complementary parameters. Hence, they should be treated simultaneously in the broad band MT interpretation.

Impedance Polar Diagrams

Once the impedance tensor Z has been found in our original (x,y,z) coordinate system, it can be rotated horizontally to any other

system (x',y',z) by an angle θ in the clockwise direction. The rotated impedance elements are given as:

$$2Z'_{xx}(\theta) = (Z_{xx}+Z_{yy}) + (Z_{xx}-Z_{yy})\cos 2\theta + (Z_{xy}+Z_{yx})\sin 2\theta \quad , \quad (31)$$

$$2Z'_{xy}(\theta) = (Z_{xy}-Z_{yx}) + (Z_{xy}+Z_{yx})\cos 2\theta - (Z_{xx}-Z_{yy})\sin 2\theta \quad , \quad (32)$$

$$2Z'_{yx}(\theta) = -(Z_{xy}-Z_{yx}) + (Z_{xy}+Z_{yx})\cos 2\theta - (Z_{xx}-Z_{xy})\sin 2\theta \quad , \quad (33)$$

$$2Z'_{yy}(\theta) = (Z_{xx}+Z_{yy}) - (Z_{xx}-Z_{yy})\cos 2\theta - (Z_{xy}+Z_{yx})\sin 2\theta \quad , \quad (34)$$

The superscript "prime" for the impedance elements is used to indicate that they are functions of θ. By horizontally rotating the original coordinate system in 3° increments from 0° to 360°, we contour the magnitude of the off-diagonal element, $|Z'_{xy}|$ and the diagonal element $|Z'_{xx}|$ of the impedance tensor. The resulting diagrams, which have been called impedance polar diagrams (Reddy et al., 1977), are presented at 0.1 Hz and 10 Hz in Figures 15 and 16 respectively. The diagonal element is normalized with respect to the off-diagonal element which in turn is normalized to its own maximum value. The polar diagrams for $|Z'_{yx}|$ and $|Z'_{yy}|$ can be obtained from $|Z'_{xy}|$ and $|Z'_{xx}|$ respectively by just a 90-degree rotation. The main advantage of these polar diagrams is that they eliminate the dependence on the orientation of coordinate system and, therefore, allow us to have an overall picture of the impedance tensor. Here, we are only dealing with the magnitude of the impedance elements, but similar polar diagrams for impedance phase could also be studied.

The polar diagrams for $|Z'_{xy}|$ in general have the shape of a

peanut. The polar diagrams for $|Z'_{xx}|$ always attain the shape of a clover leaf. Along the symmetry lines of the model these lobes are symmetric, a characteristic of a two-dimensional earth (Reddy et al., 1977). Away from the symmetry lines, these diagrams start to have an elongation, and their magnitudes become greater, particularly at the lower frequency. Therefore, with a polar diagram, one can immediately recognize a three dimensional structure from a single measuring site, unless it is located on a line of symmetry above the structure. Of course, this recognition can be more easily achieved at a lower frequency as shown by the comparison of Figures 15 and 16.

Tipper

A relationship similar to (23) or (24) can be written between the vertical magnetic field component, H_z, and the horizontal magnetic field components H_x and H_y.

$$H_z = AH_x + BH_y \quad , \qquad (35)$$

where A and B are unknown complex coefficients, which are called magnetic transfer functions. To solve for A and B, we again need two different source polarizations. This pair of coefficients can be thought of as operating on the horizontal magnetic field and tipping part of it into the vertical. For that reason, (A, B) is also called the "tipper" (Vozoff, 1972). Its magnitude is

$$|T| = \{|A|^2 + |B|^2\}^{1/2} \quad . \qquad (36)$$

The tipper direction, ϕ , here is defined as the angle measuring

Figures 11 and 12 show surface contours of the apparent resistivity along the original coordinate system at 0.1 Hz and 10 Hz respectively. On the coordinate axes, on-diagonal apparent resistivities, ρ_{xx} and ρ_{yy} are zero, which means the fields could be decomposed into the E and E mode as in the 2D case. This happens as a coincidence because our coordinate system is right on the symmetry lines of the earth model. Near the corner, ρ_{xx} and ρ_{yy} approach their maximum which is purely due to the three dimensionality. Because three dimensionality is more important at the lower frequency, ρ_{xx} and ρ_{yy} are much greater at 0.1 Hz than they are at 10 Hz. Also because of the symmetry of the model, contours of ρ_{xy} and ρ_{yx} have a similar pattern except for a 90-degree rotation.

The corresponding phase contours are shown in Figures 13 and 14. xx and yy are neglected on the coordinate axes where the on-diagonal impedance elements, Z_{xx} and Z_{yy} are near-zero unstable numbers. Unlike apparent resistivity, phase contours do not explicitly show the three dimensionality. Furthermore, we see stronger variation, which means higher resolving power, of phase at the higher frequency in contrast to the small variation diagnostic of apparent resistivity at the higher frequency. This suggests that apparent resistivity and phase are really two complementary parameters. Hence, they should be treated simultaneously in the broad band MT interpretation.

Impedance Polar Diagrams

Once the impedance tensor Z has been found in our original (x,y,z) coordinate system, it can be rotated horizontally to any other

clockwise from the x axis along which the coherency between vertical and the horizontal magnetic field is at its maximum. It can be obtained explicitly by the formula (Jupp and Vozoff, 1976)

$$\phi = \frac{(A_r^2+B_r^2)\tan^{-1}(B_r/A_r) + (A_i^2+B_i^2)\tan^{-1}(B_i/A_i)}{|T|^2} \qquad (37)$$

where subscript 'r' means the 'real part' and 'i' means the 'imaginary' part of a complex number.

We have drawn the tipper direction as an arrow in the polar diagrams on Figures 15 and 16. The length of the arrow represents the magnitude of the tipper, and it has been normalized with respect to the maximum value on the whole grid. In the two dimensional case, this direction should be perpendicular to the true strike direction of the structure. However, for our three dimensional prism, the direction varies and always points away from the conductive prism.

Practically, we think the tipper direction is a very useful parameter. By plotting it at a few points on the surface, we can easily locate the area below which the conductive zone lies. This not only can help select a drilling location, but also can show where more detailed MT work should be carried out. Furthermore, we have found the above unique characteristic of tipper direction almost has not been affected by the frequency, at least between 0.1 Hz and 10 Hz.

Figure 17 presents the contour of tipper magnitude at 0.1 Hz and 10 Hz, which represents the relative strength of vertical magnetic field (Vozoff, 1972). Its values along "x" axis are larger than those

along the corresponding "y" axis. This is because currents tend to flow along the elongation direction of the prism. At the higher frequency, tipper magnitude is much greater, and its contour tends to outline the boundary of the prism.

Principal Directions

There are many ways to define the principal directions derived from the impedance tensor. For example, maximize $|Z'_{xy}|^2 + |Z'_{yx}|^2$, minimize $|Z'_{xx}|^2 + |Z'_{yy}|^2$, maximize $|Z'_{xy}|$ or $|Z'_{yx}|$, minimize $|Z'_{xx}|$ or $|Z'_{yy}|$, maximize $|Z'_{xy} + Z'_{yx}|$, etc. They all give the principal directions of the structure if the earth is two dimensional. In our 3D case, though, these methods do not give the same results. This is because the trace of all the impedance elements on the complex plane is an ellipse, all having the same orientation, instead of a line or a point as in the 2D or 1D case respectively (Word et. al., 1970). We have chosen the method of Sims et. al. (1969) of maximizing the absolute value of the sum of the off-diagonal elements, mainly because their method always gives two perpendicular directions which correspond to the major axis of the ellipse - a unique characteristic of the impedance tensor.

The angle, θ_o, at which $|Z'_{xy} + Z'_{yx}|$ has zero first derivative can be derived analytically (Sims et. al, 1969).

$$\theta_o = 1/4\tan^{-1}\left[\frac{2(R_1R_2 + I_1I_2)}{(R_1^2+I_1^2 - R_2^2-I_2^2)}\right] \qquad (38)$$

with R_1, R_2 and I_1, I_2 are the real and imaginary parts of $(Z_{xx} - Z_{yy})$ and $(Z_{xy} + Z_{yx})$ respectively. Between zero and 360 degrees, there are

eight θ's which can satisfy equation (38), but only four of them give the maximum value of $|Z_{xy}' + Z_{yx}'|$ and they form two principal directions perpendicular to each other.

In Figures 15 and 16, the single straight line at each grid point represents the principal direction farthest from the direction of tipper. If the earth were two dimensional, this direction would coincide with the strike direction. For our 3D prismatic model, this direction varies around the prism and tends to parallel the nearest side of the prism. Hence, estimation of the electrical strike direction from a single measuring site for an elongated 3D body could be misleading since it depends upon where the observer is located. Once again, just like the tipper direction, principal directions are not affected much by changing the frequency.

Skew

The three-dimensionality parameter 'skew' is defined as

$$\text{skew} = \frac{|Z_{xx}' + Z_{yy}'|}{|Z_{xy}' - Z_{yx}'|} \qquad (39)$$

As noted from equation (31) to (34), both $(Z_{xx} + Z_{yy})$ and $(Z_{xy} - Z_{yx})$ are independent of θ, skew does not depend on the measuring axes. Figure 18 shows the surface contours of skew at 0.1 Hz and 10 Hz. Skew must be zero for one and two dimensional structures. But it is also zero along the lines of symmetry of our 3D model. Consistent with the contours of on-diagonal apparent resistivities, ρ_{xx} and ρ_{yy} along the original coordinate system, three-dimensionality has been revealed more obviously at the lower frequency. However, its maximum

occurs somewhat off the corner as opposed to the on-diagonal apparent resistivities which have their maximum right above the corner. We think this is due to the asymmetry between Z_{xy} and Z_{yx} which were introduced in the calculation of skew.

Ellipticity

As we have said, all the impedance elements trace out similar ellipses on a complex plane as we horizontally vary the orientation of the coordinate system. The ellipticity, which is the ratio of minor to major axis of the ellipse, can be obtained analytically (Word et. al., 1970).

$$\text{Ellipticity} = \frac{|(Z_{xx}-Z_{yy})\text{Cos } 2\theta_o + (Z_{xy}+Z_{yx})\text{Sin } 2\theta_o|}{|(Z_{xy}+Z_{yx})\text{Cos } 2\theta_o + (Z_{xx}-Z_{yy})\text{Sin } 2\theta_o|} \quad , \quad (40)$$

where θ_o can be any of the principal directions derived previously.

Ellipticity, like skew, is also a three-dimensionality indicator because it is zero for one- and two-dimensional models. Figure 19 shows the surface contour of ellipticity at 0.1 Hz and 10 Hz. The contour of ellipticity has a very similar pattern as that of skew except that they vary differently with frequency. While skew shows three-dimensionality more obviously at the higher frequency, ellipticity does that at the lower frequency. Hence, these two parameters are a pair of complementary three-dimensionality indicators.

CONCLUSIONS

Our results show that the forward modeling of three-dimensional structures can be achieved successfully by our integral equation method. Since pulse basis functions are used, we have not been able to model accurately very shallow or large subsurface features as they require a great number of cells which our computer can not handle at the present time.

Usually, MT measurements are made in the frequency range 0.001 Hz to 10 Hz. In this paper we have shown that 1D or 2D interpretation over a three-dimensional earth can be misleading, particularly using the lower half of the above frequency range. Hence, in many cases, 3D models are required for interpreting MT data.

By presenting various MT parameters due to a simple 3D model, we have recognized two pairs of complementary parameters, namely, apparent resistivity and phase, skew and ellipticity. They should be examined simultaneously for any broad band MT exploration. All the MT parameters have clearly shown three-dimensionality. Hence, the recognition of a three-dimensional structure from the field data should not be difficult.

Although an overall 3D MT interpretation is still not practical, combined 2D and 3D modeling could be applied to yield a gross 3D structure, which is composed of a cross section and its strike extent. In doing so, we suggest that the cross section be obtained from higher frequency 2D $E_{\perp}$ mode modeling, and that the strike extent be derived by matching with lower frequency $E_{\parallel}$ mode results due to corresponding

3D models. In addition, we have indicated that some simple 3D features, e.g., location above conductive zone, corners, and symmetry lines, can be easily recognized.

ACKNOWLEDGEMENTS

This work was funded by the Department of Energy, Division of Geothermal Energy, contract no. EG-78-C-07-1701. The authors wish to thank Dr. Charles M. Swift, Jr. for valuable comments. We thank John A. Stodt for providing us the 2D finite element forward modeling program and William R. Petrick for providing us program to calculate the 1D results. Some helpful discussions were held with P. Wannamaker and J. A. Stodt who are the first author's officemates.

REFERENCES

Butler, C. M. and Wilton, D. R., 1975, Analysis of various numerical techniques applied to thin-wire scatterers: IEEE Trans. on Ant. and Prop., V AP-23, no. 4, p. 534-540.

Harrington, R. F., 1968, Field computation by moment methods: New York, MacMillan Co.

Hohmann, G. W., 1975, Three-dimensional induced polarization and electromagnetic modeling: Geophysics, v. 40, no. 2, p. 309-324.

Hohmann, G. W. and S. C. Ting, 1978, Three-Dimensional Magnetotelluric Modeling, ESL Final Report 77-15, DOE Contract EY-76-S-07-1601, July, 48 p.

Jones, F. W., 1974, The perturbation of geomagnetic fields by two-dimensional and three-dimensional conductivity inhomogeneities: Pure & Applied Phys., v. 112, p. 793-800.

Jones, F. W. and Vozoff, K., 1978, The calculation of magnetotelluric quantities for three-dimensional conductivity inhomogeneities: Geophysics, v. 43, no. 6, p. 1167-1175.

Jupp, D. L. and Vozoff, K., 1976, Discussion on "The Magnetotelluric method in the exploration of sedimentary basins" by K. Vozoff: Geophysics, v. 41, no. 2, p. 325-328.

Mayer, W. H., 1976, Computer modelling of electromagnetic prospecting methods: Ph.D. thesis Univ. of Calif., Berkeley.

Miller, E. K., and Deadrick, F. J., 1975, Some computational aspects of thin wire modeling in Numerical and asymptotic techniques in electromagnetics; R. Mittra, ed.: New York, Springer-Verlag.

Reddy, I. K., Rankin, D., and Phillips, R. J., 1977, Three-dimensional modeling in magnetotelluric and magnetic variational sounding: Geophys. J. R. Astr. Soc., v. 51, p. 313-325.

Rijo, L., 1977, Modeling of electric and electromagnetic data: Ph.D. thesis, Univ. of Utah.

Sims, W. E., and Bostick, F. K., Jr., 1969, Methods of Magnetotelluric analysis: EGRL Tech. Rep. No. 58, Univ. of Texas at Austin.

Tai, Chen-To, 1971, Dyadic Green's functions in electromagnetic theory: Scranton, International Textbook Co.

Vozoff, K., 1972, The Magnetotelluric method in the exploration of sedimentary basins, Geophysics, v. 37, no. 2, p. 98-141.

Wannamaker, P., 1978, Magnetotelluric investigations at the Roosevelt Hot Springs KGRA and Mineral Mountains, Utah: Univ. of Utah, DOE/DGE Rpt. 78-1701.a.6.1.

Wannamaker, P., et al., 1979, 2-D and 3-D Magnetotelluric Modeling with applications to Crustal Structure and Reservoir Assessment at the Roosevelt Hot Springs, KGRA, Utah. Presented at the 49th annual international SEG meeting, New Orleans, Louisiana.

Weidelt, P., 1975, Electromagnetic induction in three-dimensional structures. Geophys. J. R. Astr. Soc., v. 41, p. 85-109.

Word, D. R., et al., 1970, An Investigation of the Magnetotelluric Tensor Impedance Method: EGRL Tech. Rep. No. 82, Univ. of Texas at Austin.

LIST OF ILLUSTRATIONS

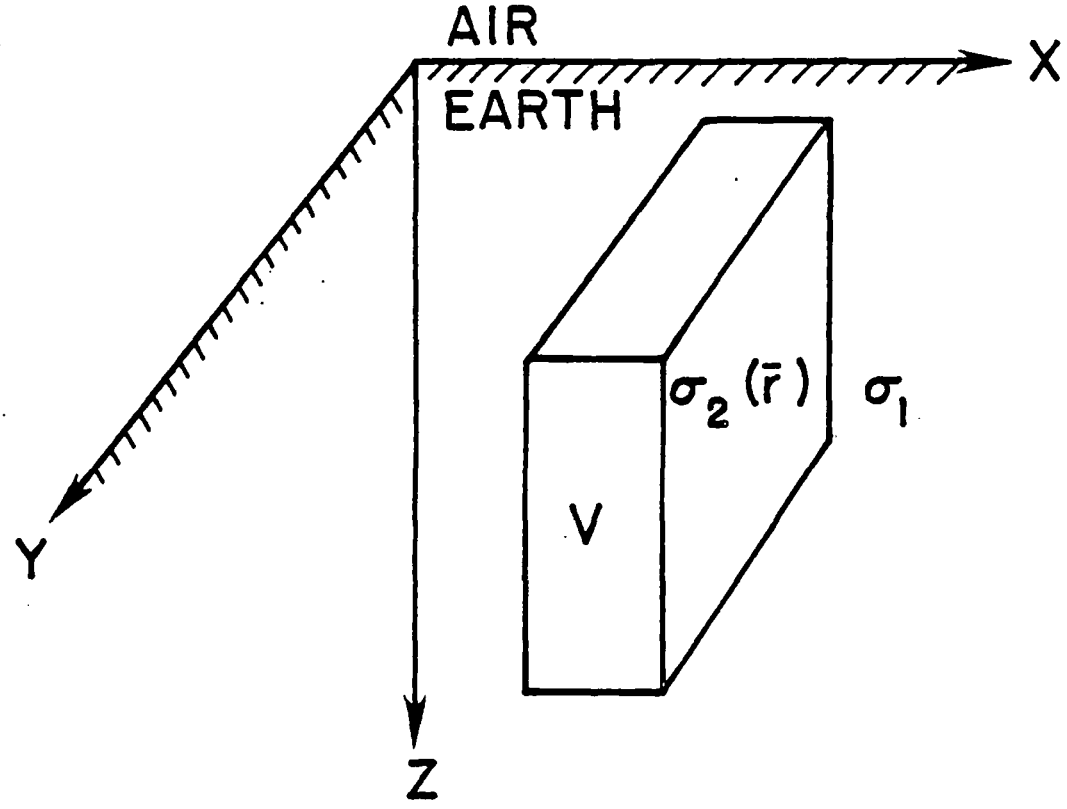

Figure 1

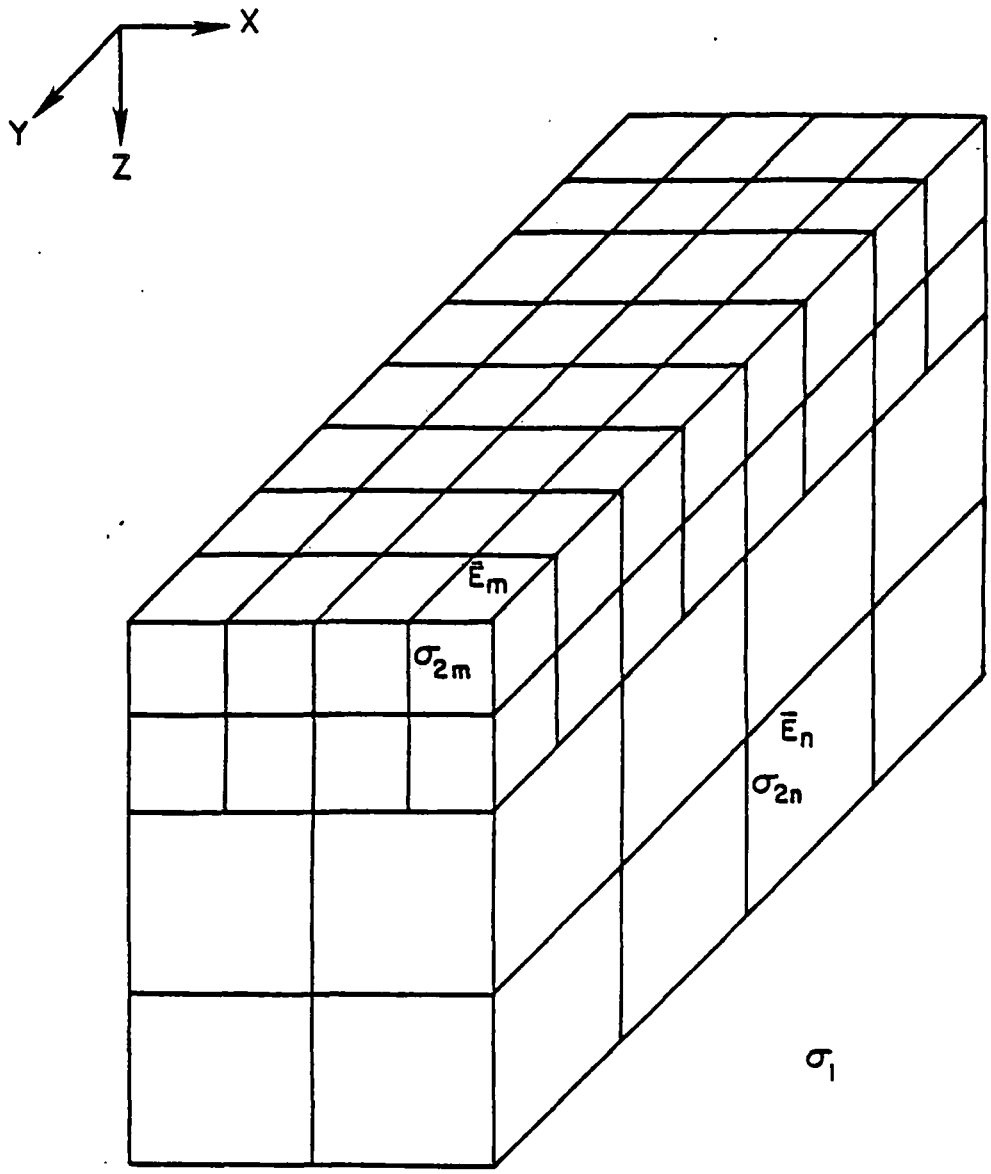

Figure 2

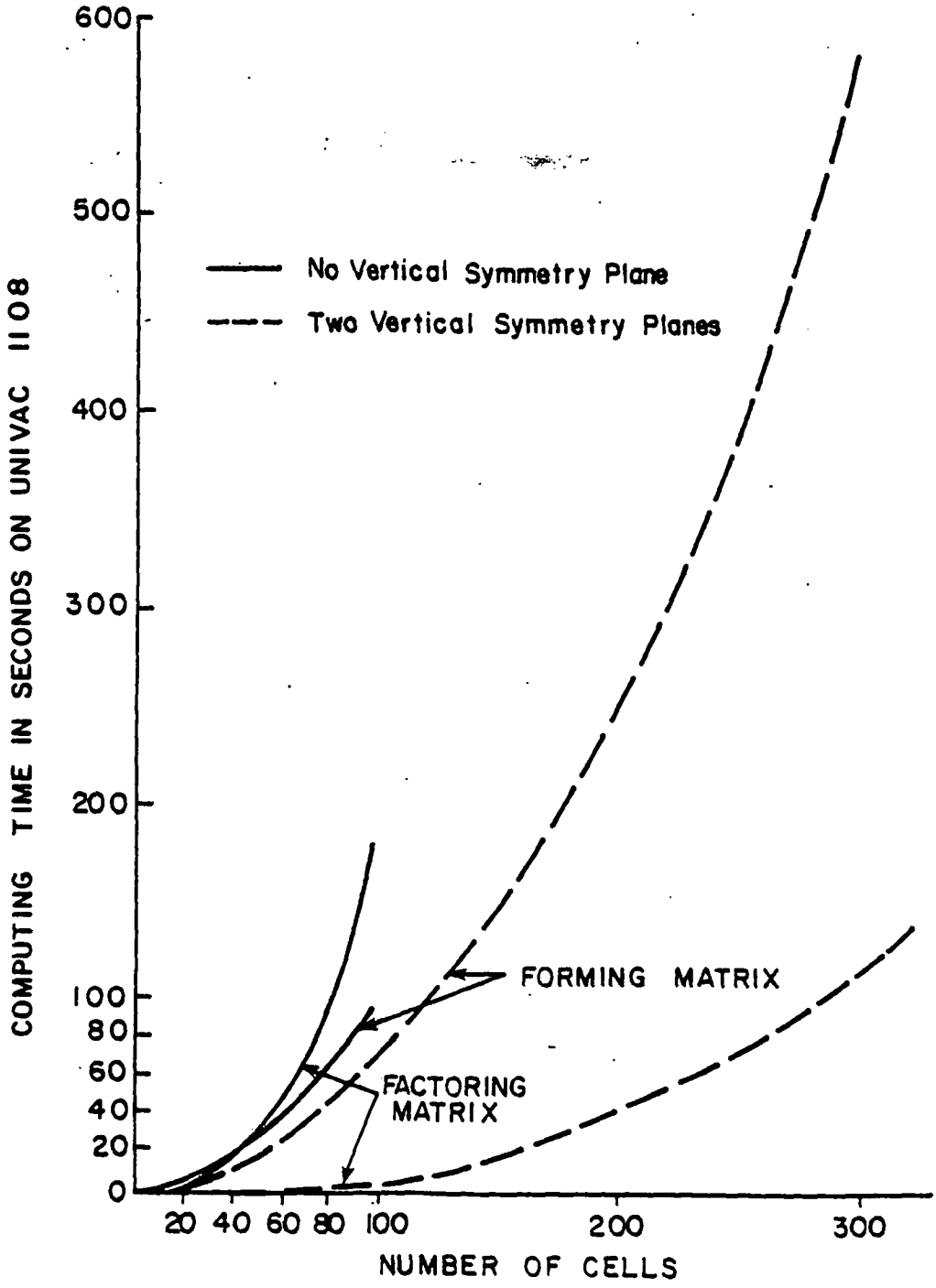
COMPUTING TIME IN SECONDS ON UNIVAC 1108
600
500
400
300
200
100
80
60
40
20
0
No Vertical Symmetry Plane
Two Vertical Symmetry Planes
FORMING MATRIX
FACTORING MATRIX
20 40 60 80 100 200 300
NUMBER OF CELLS

Figure 3

LEGEND

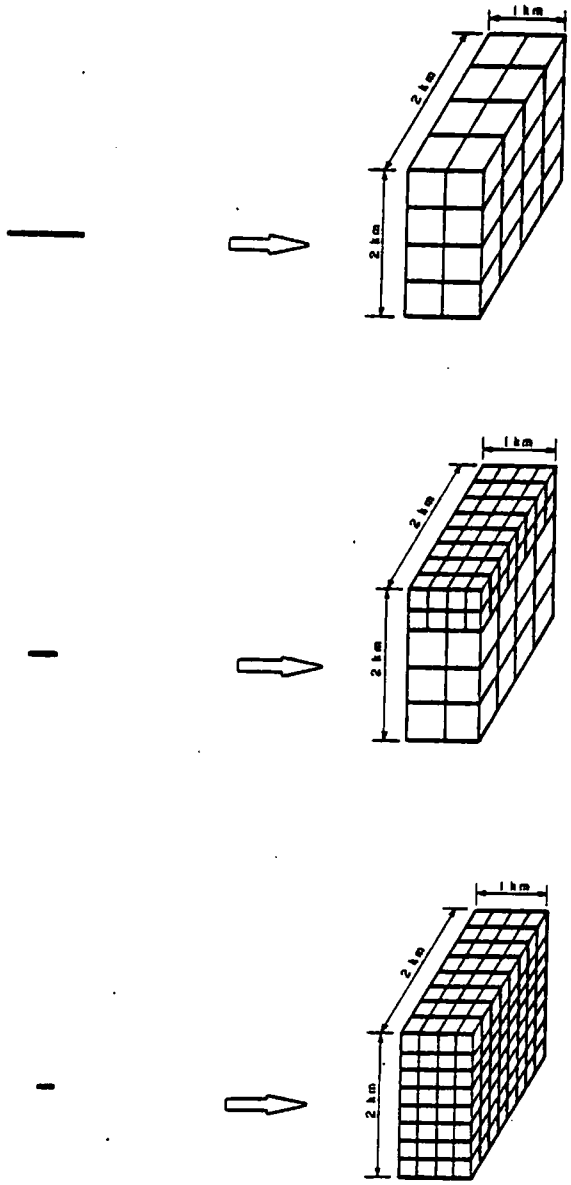

Figure 4

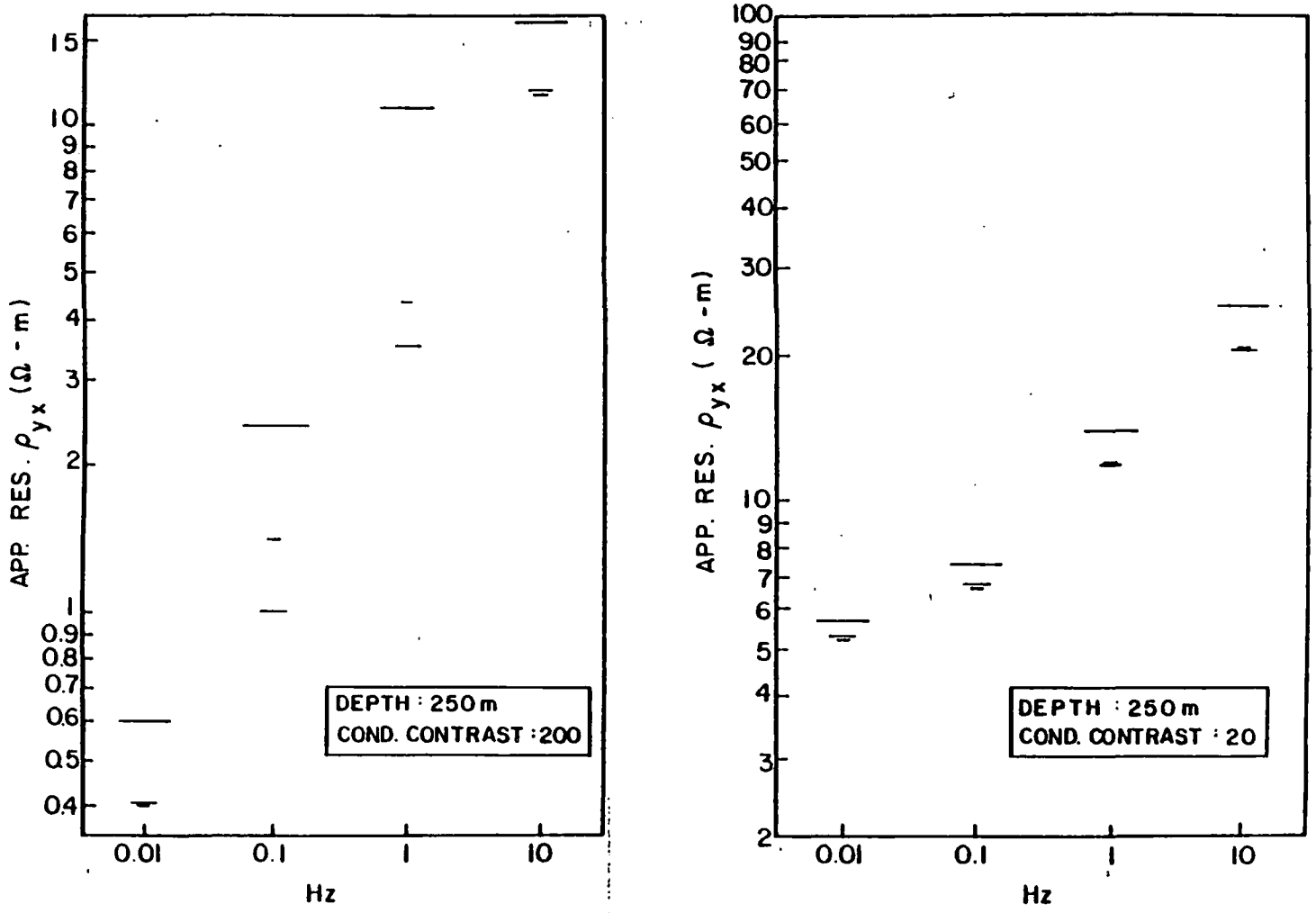
APP. RES. ρ_{yx} (Ω - m)
15
10
9
8
7
6
5
4
3
2
1
0.9
0.8
0.7
0.6
0.5
0.4
0.01
0.1
1
10
Hz
DEPTH : 250 m
COND. CONTRAST : 200
APP. RES. ρ_{yx} (Ω - m)
100
90
80
70
60
50
40
30
20
10
9
8
7
6
5
4
3
2
0.01
0.1
1
10
Hz
DEPTH : 250 m
COND. CONTRAST : 20

Figure 5a

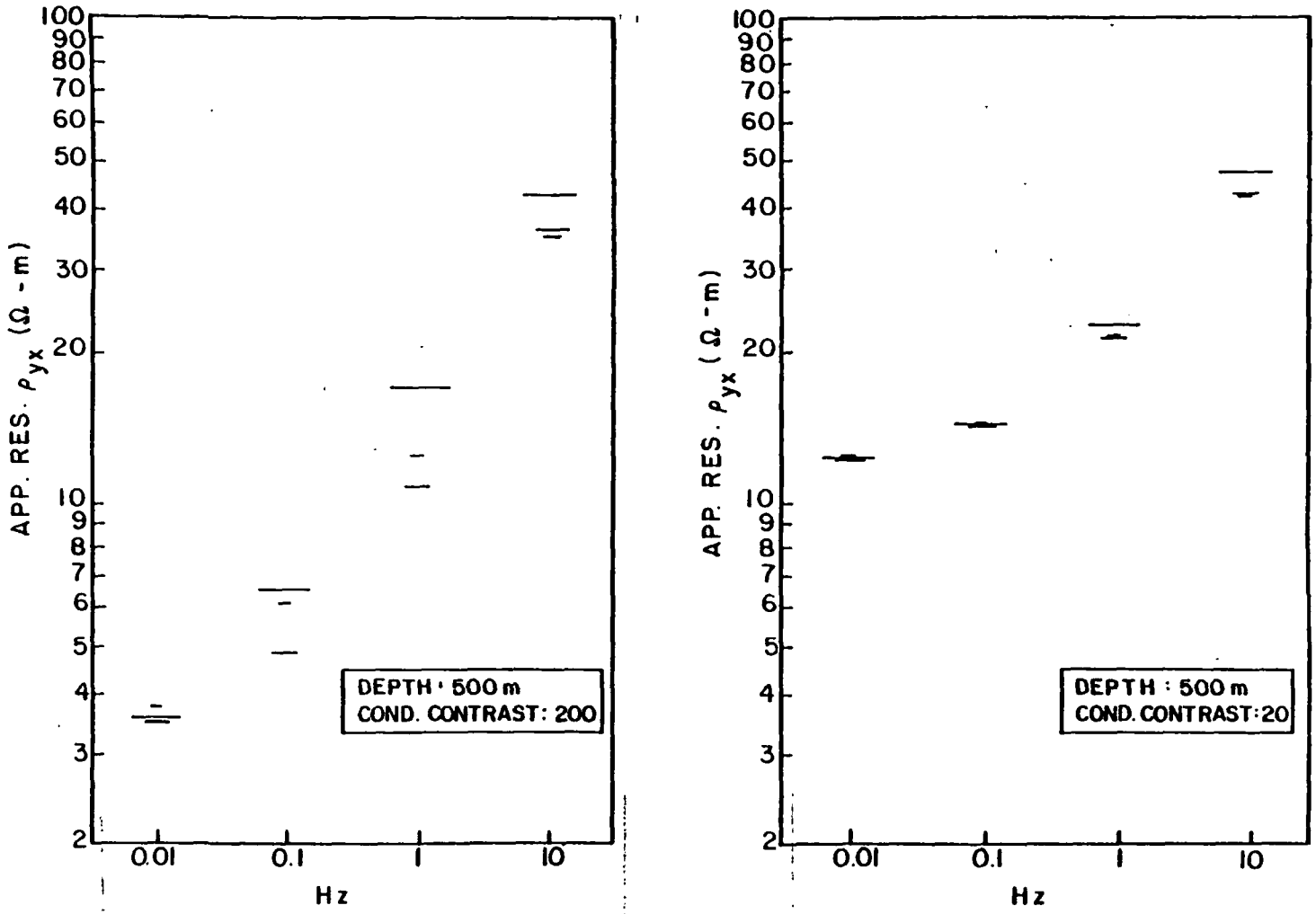
APP. RES. ρ_{yx} (Ω - m)
100
90
80
70
60
50
40
30
20
10
9
8
7
6
5
4
3
2
0.01
0.1
1
10
Hz
DEPTH : 500 m
COND. CONTRAST: 200
DEPTH : 500 m
COND. CONTRAST: 20

Figure 5b

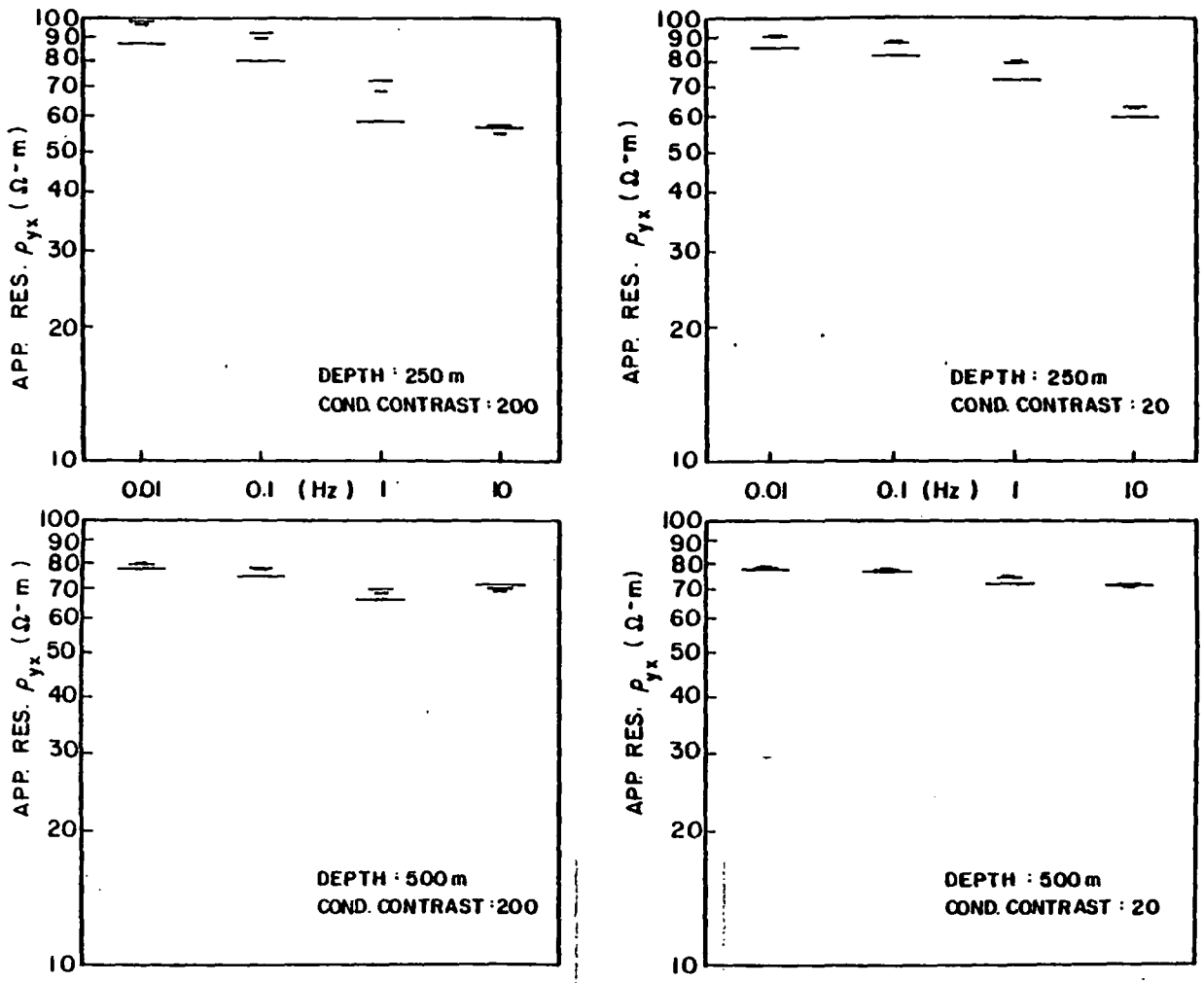
APP. RES. ρ_{yx} (Ω-m)
100
90
80
70
60
50
40
30
20
10
0.01
0.1
(Hz)
1
10
DEPTH : 250 m
COND. CONTRAST : 200
DEPTH : 250m
COND. CONTRAST : 20
DEPTH : 500 m
COND. CONTRAST : 200
DEPTH : 500 m
COND. CONTRAST : 20

Figure 6

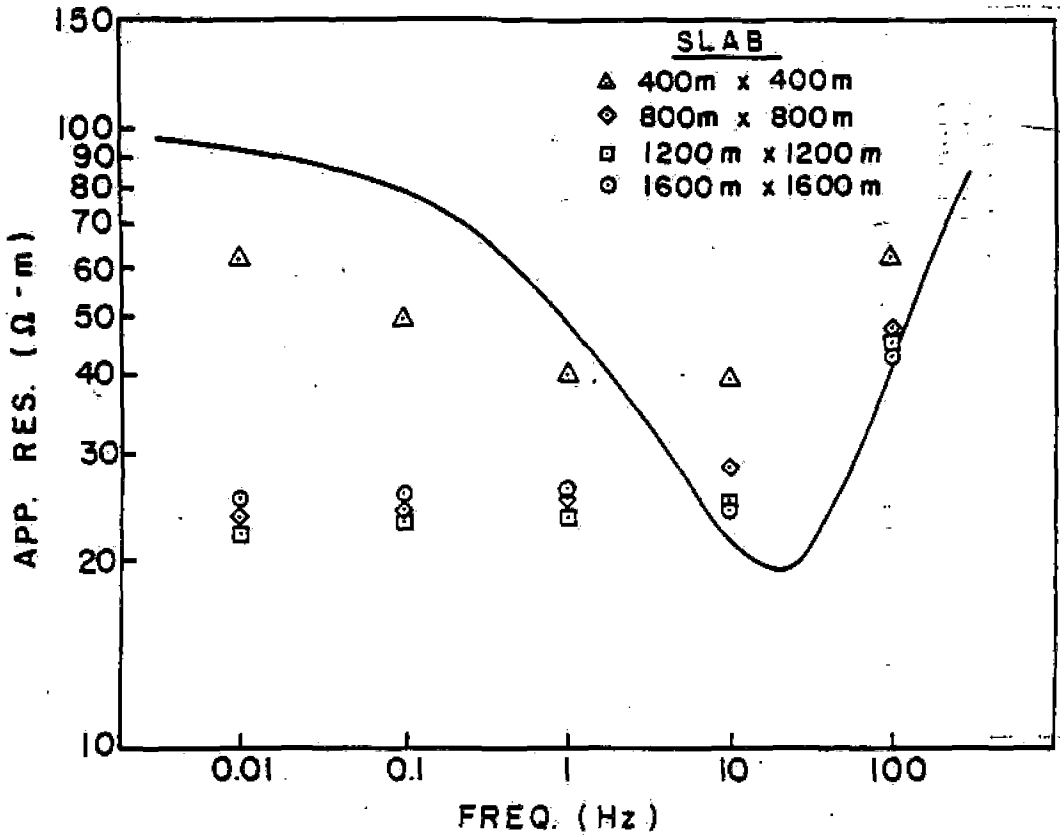
SLAB
400m x 400m
800m x 800m
1200m x 1200m
1600m x 1600m
APP. RES. (Ω-m)
150
100
90
80
70
60
50
40
30
20
10
0.01
0.1
1
10
100
FREQ. (Hz)

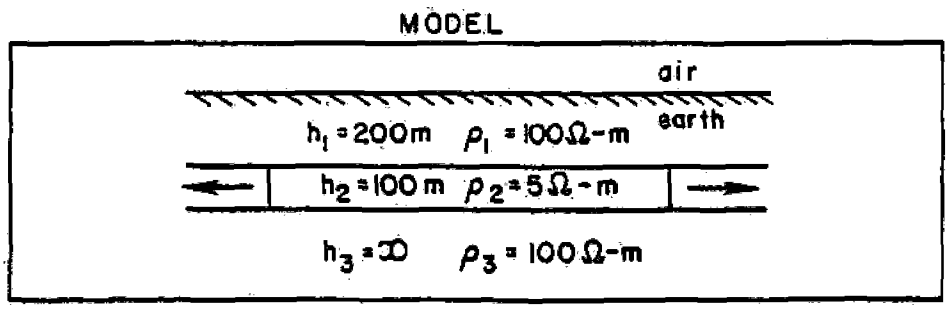
MODEL
air
earth
h_1 = 200m ρ_1 = 100Ω-m
h_2 = 100 m ρ_2 = 5Ω-m
h_3 = ∞ ρ_3 = 100Ω-m

Figure 7

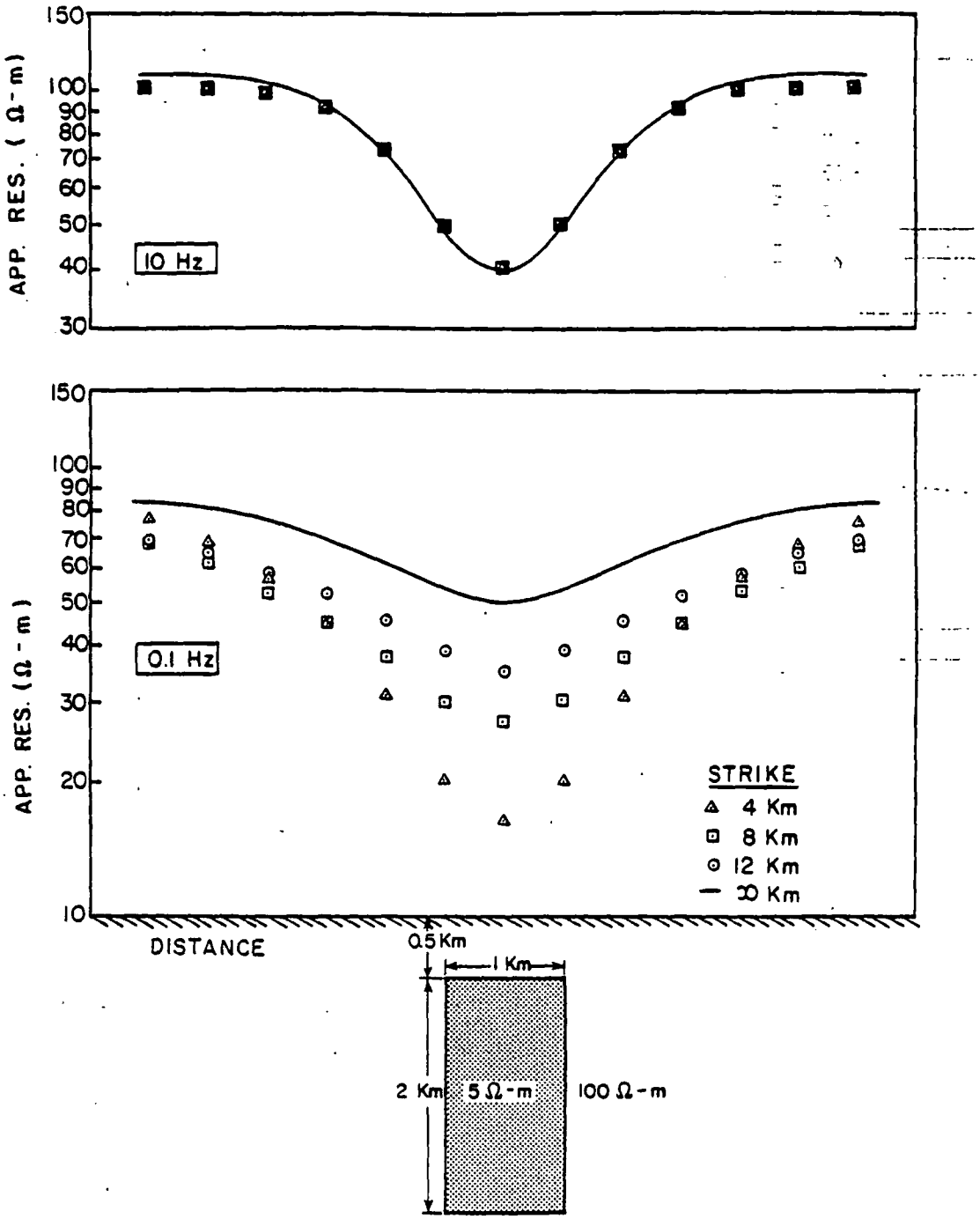
150
100
90
80
70
60
50
40
30
APP. RES. (Ω - m)
10 Hz
150
100
90
80
70
60
50
40
30
20
10
APP. RES. (Ω - m)
0.1 Hz
STRIKE
4 Km
8 Km
12 Km
∞ Km
DISTANCE
0.5 Km
1 Km
2 Km
5 Ω - m
100 Ω - m

Figure 8

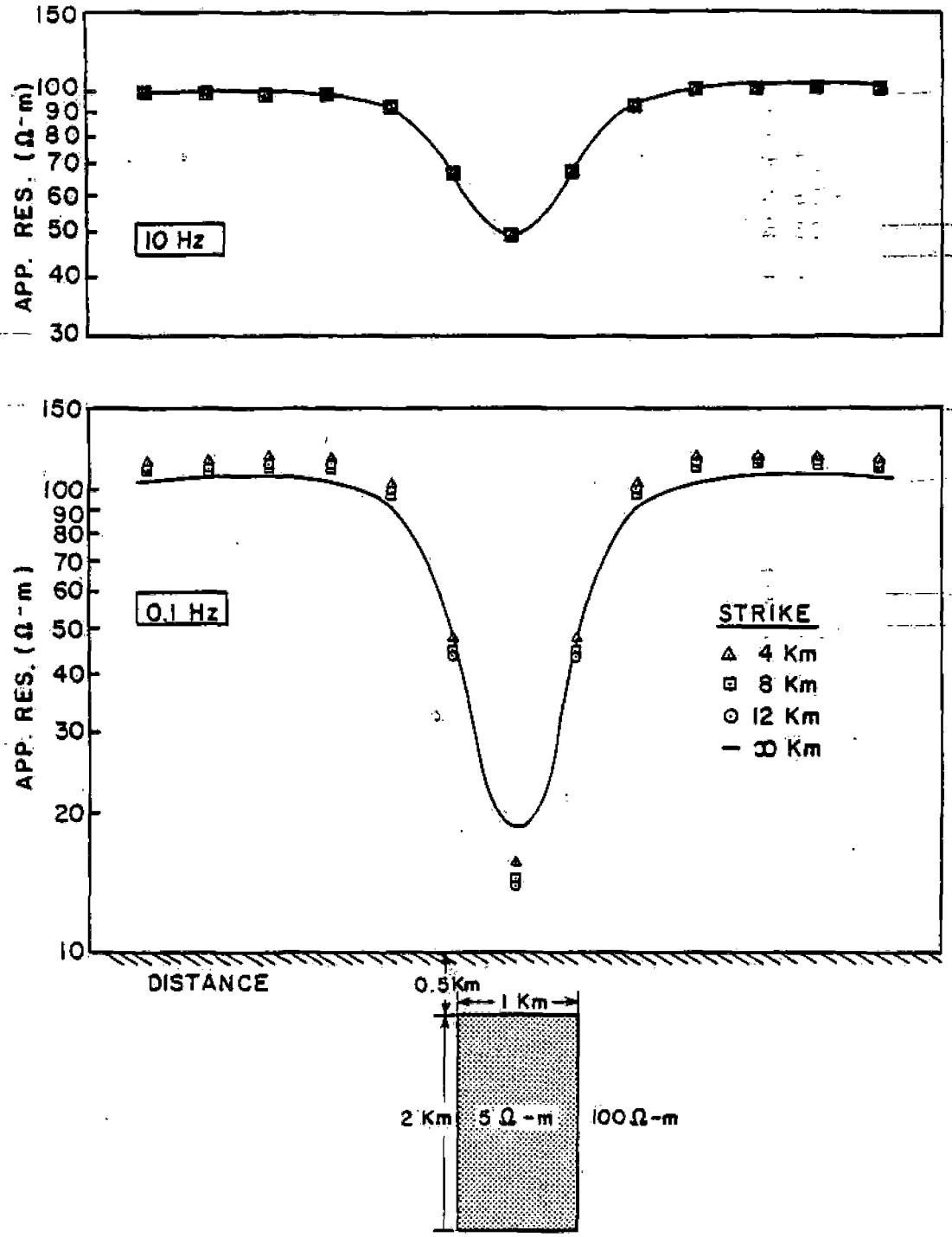
150
100
90
80
70
60
50
40
30
APP. RES. (Ω-m)
10 Hz
150
100
90
80
70
60
50
40
30
20
10
APP. RES. (Ω-m)
0.1 Hz
STRIKE
4 Km
8 Km
12 Km
∞ Km
DISTANCE
0.5Km
1 Km
2 Km
5 Ω-m
100Ω-m

Figure 9

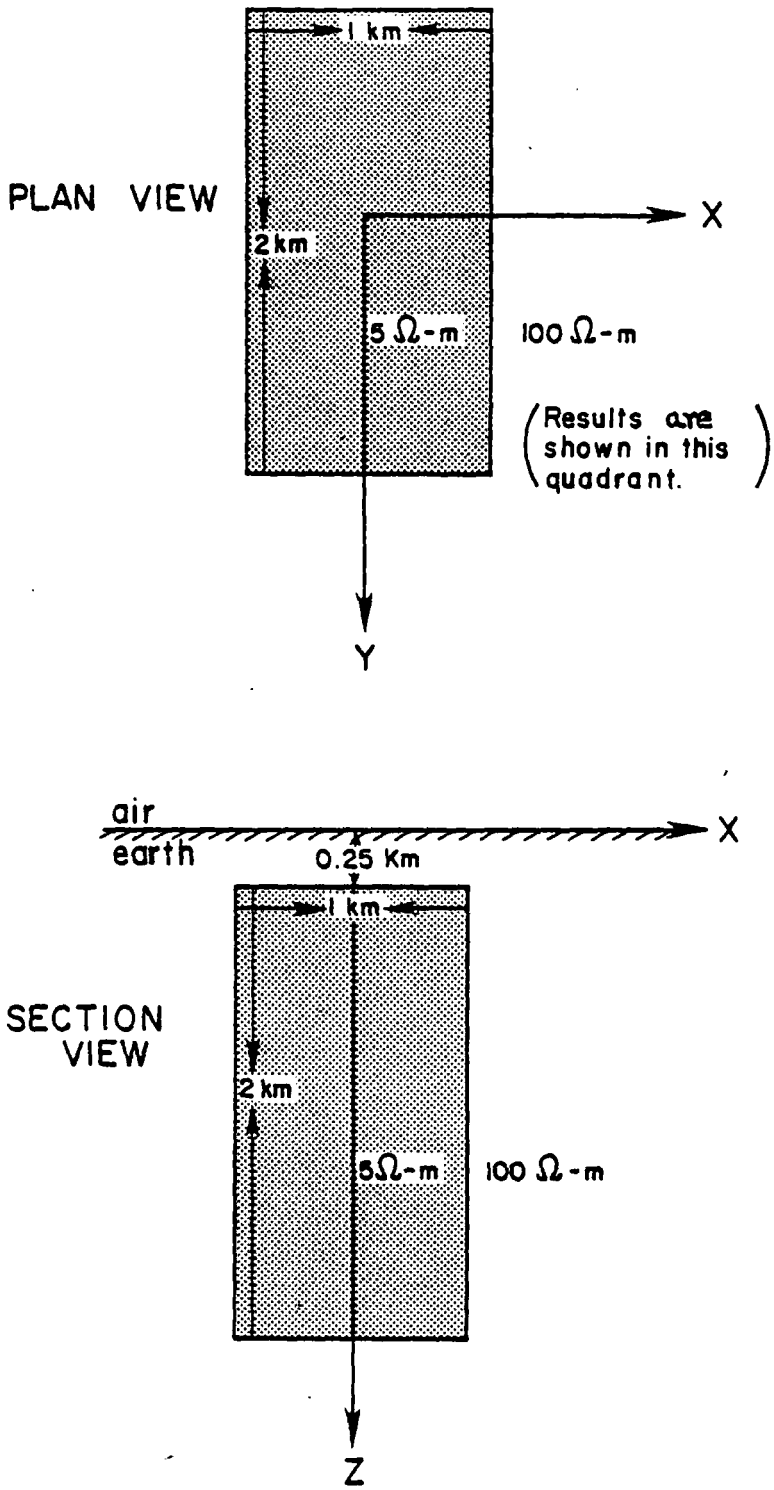
PLAN VIEW
1 km
2km
X
5 Ω-m
100 Ω-m
(Results are shown in this quadrant.)
Y
air
earth
X
0.25 Km
SECTION VIEW
1 km
2 km
5Ω-m
100 Ω-m
Z

Figure 10

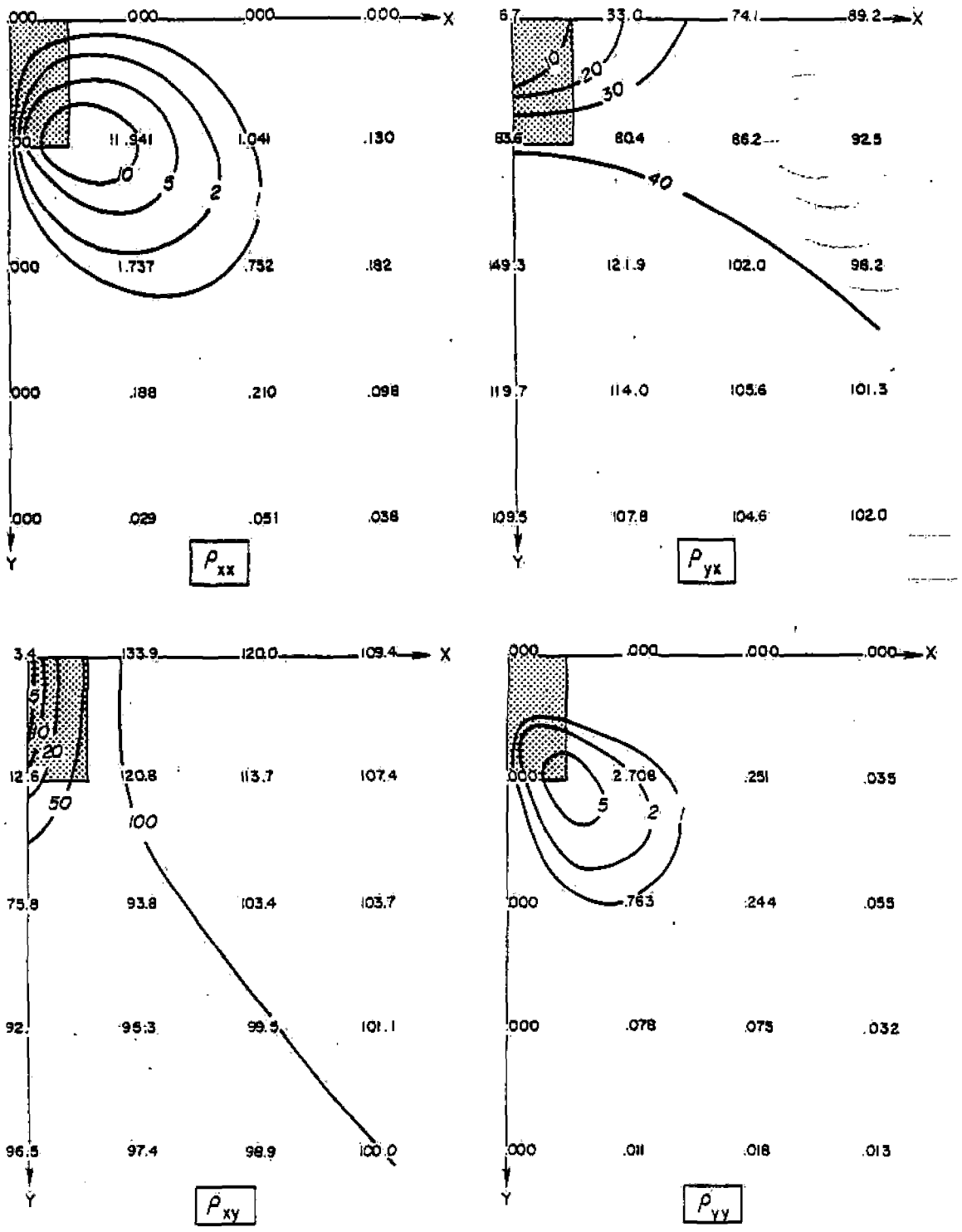
.000 .000 .000 .000 X
11.941 1.041 .130
10
5
2
.000 1.737 .752 .182
.000 .188 .210 .098
.000 .029 .051 .038
Y
ρ_{xx}
6.7 33.0 74.1 89.2 X
10
20
30
83.6 80.4 86.2 92.5
40
149.3 121.9 102.0 98.2
119.7 114.0 105.6 101.3
109.5 107.8 104.6 102.0
Y
ρ_{yx}
3.4 133.9 120.0 109.4 X
5
10
20
12.6 120.8 113.7 107.4
50
100
75.8 93.8 103.4 103.7
92. 95.3 99.5 101.1
96.5 97.4 98.9 100.0
Y
ρ_{xy}
.000 .000 .000 .000 X
.000 2.708 .251 .035
5
2
.000 .763 .244 .055
.000 .078 .075 .032
.000 .011 .018 .013
Y
ρ_{yy}

Figure 11

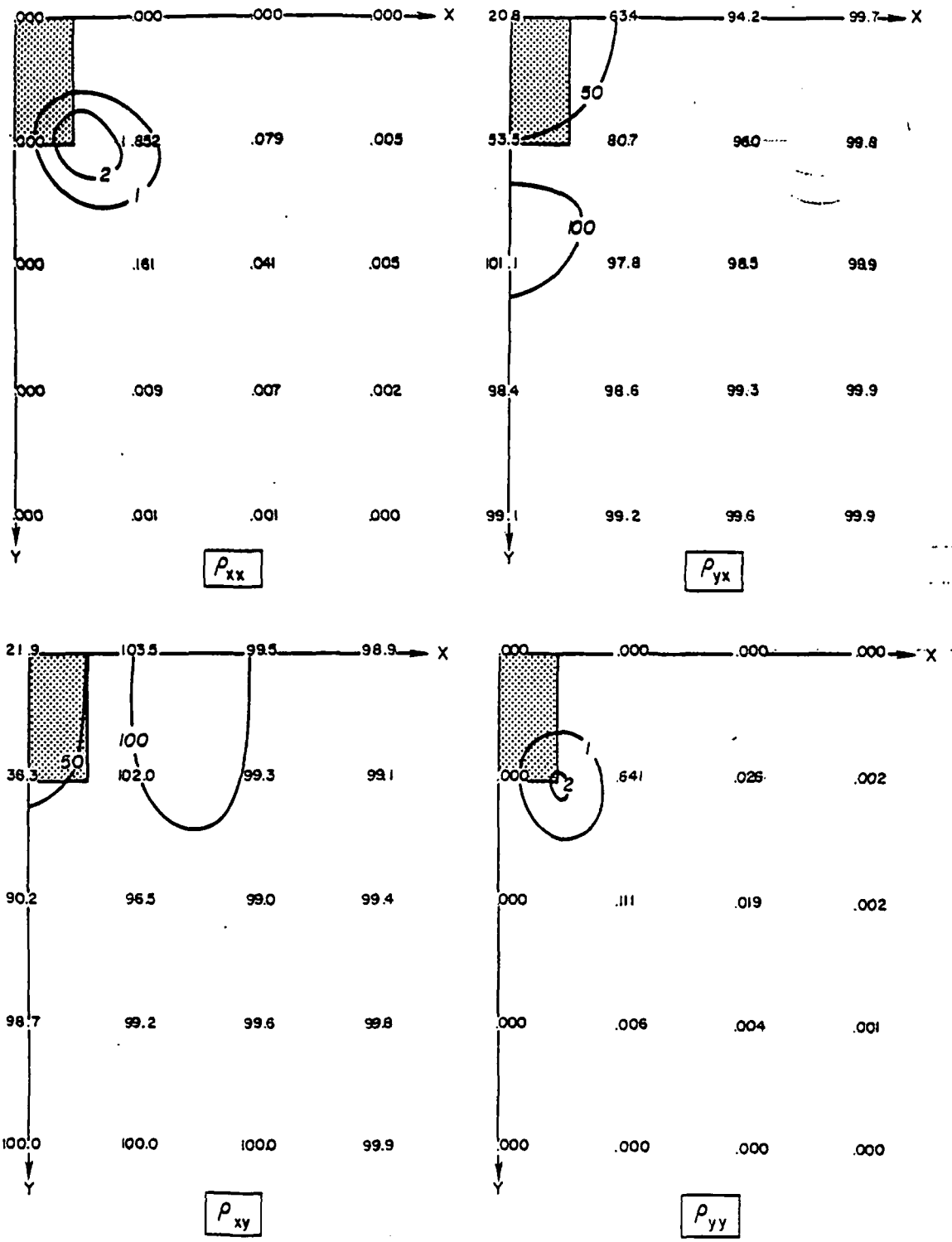
.000 .000 .000 .000 X
.000 .852 .079 .005
2
1
.000 .161 .041 .005
.000 .009 .007 .002
.000 .001 .001 .000
Y
ρ_{xx}
20.8 63.4 94.2 99.7 X
50
53.5 80.7 96.0 99.8
100
101.1 97.8 98.5 99.9
98.4 98.6 99.3 99.9
99.1 99.2 99.6 99.9
Y
ρ_{yx}
21.9 103.5 99.5 98.9 X
100
50
36.3 102.0 99.3 99.1
90.2 96.5 99.0 99.4
98.7 99.2 99.6 99.8
100.0 100.0 100.0 99.9
Y
ρ_{xy}
.000 .000 .000 .000 X
1
.000 .641 .026 .002
2
.000 .111 .019 .002
.000 .006 .004 .001
.000 .000 .000 .000
Y
ρ_{yy}

Figure 12

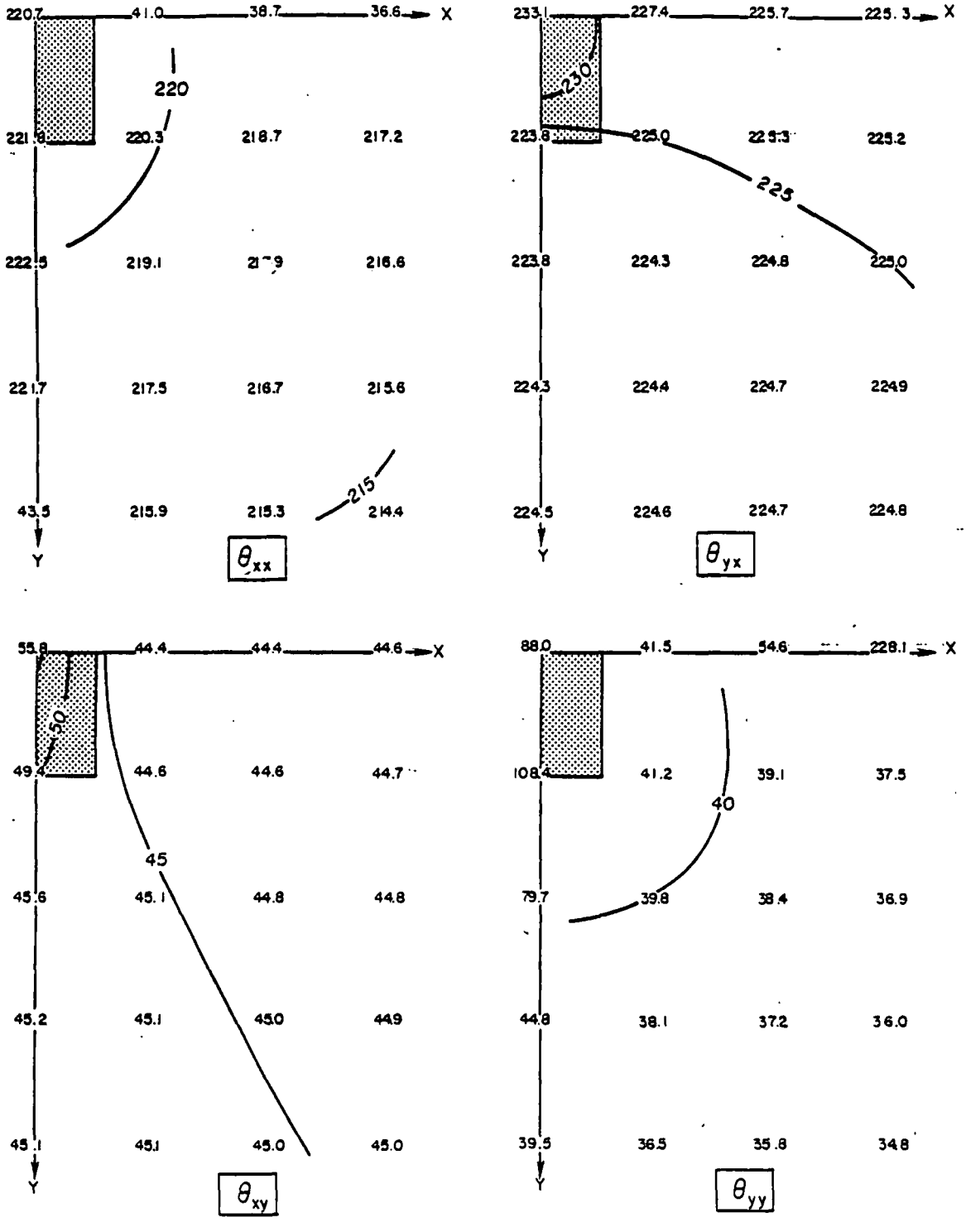
220.7
41.0
38.7
36.6
X
220
221.9
220.3
218.7
217.2
222.5
219.1
216.6
221.7
217.5
216.7
215.6
215
43.5
215.9
215.3
214.4
Y
θ_{xx}
233.1
227.4
225.7
225.3
X
230
223.8
225.0
225.2
225
223.8
224.3
224.8
225.0
224.3
224.4
224.7
224.9
224.5
224.6
224.7
224.8
Y
θ_{yx}
55.8
44.4
44.4
44.6
X
50
49.4
44.6
44.6
44.7
45
45.6
45.1
44.8
44.8
45.2
45.1
45.0
44.9
45.1
45.1
45.0
45.0
Y
θ_{xy}
88.0
41.5
54.6
228.1
X
108.4
41.2
39.1
37.5
40
79.7
39.8
38.4
36.9
44.8
38.1
37.2
36.0
39.5
36.5
35.8
34.8
Y
θ_{yy}

Figure 13

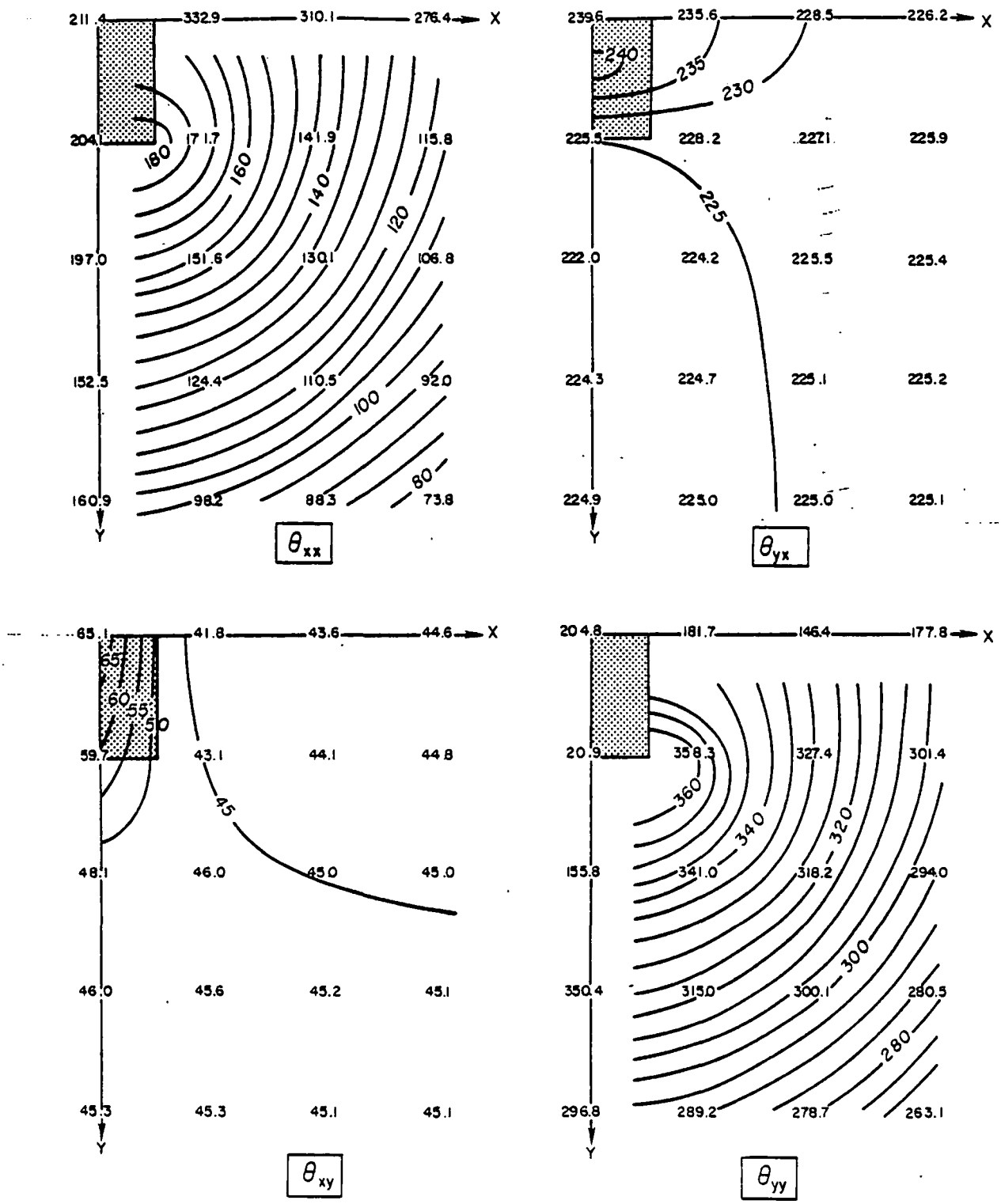
211.4
332.9
310.1
276.4
X
204
171.7
141.9
115.8
180
160
140
120
197.0
151.6
130.1
106.8
152.5
124.4
110.5
92.0
100
160.9
98.2
88.3
73.8
80
Y
θxx
239.6
235.6
228.5
226.2
X
240
235
230
225.5
228.2
227.1
225.9
225
222.0
224.2
225.5
225.4
224.3
224.7
225.1
225.2
224.9
225.0
225.0
225.1
Y
θyx
65.1
41.8
43.6
44.6
X
65
60
55
50
59.7
43.1
44.1
44.8
45
48.1
46.0
45.0
45.0
46.0
45.6
45.2
45.1
45.3
45.3
45.1
45.1
Y
θxy
204.8
181.7
146.4
177.8
X
20.9
358.3
327.4
301.4
360
340
320
155.8
341.0
318.2
294.0
350.4
315.0
300.1
280.5
300
280
296.8
289.2
278.7
263.1
Y
θyy

Figure 14

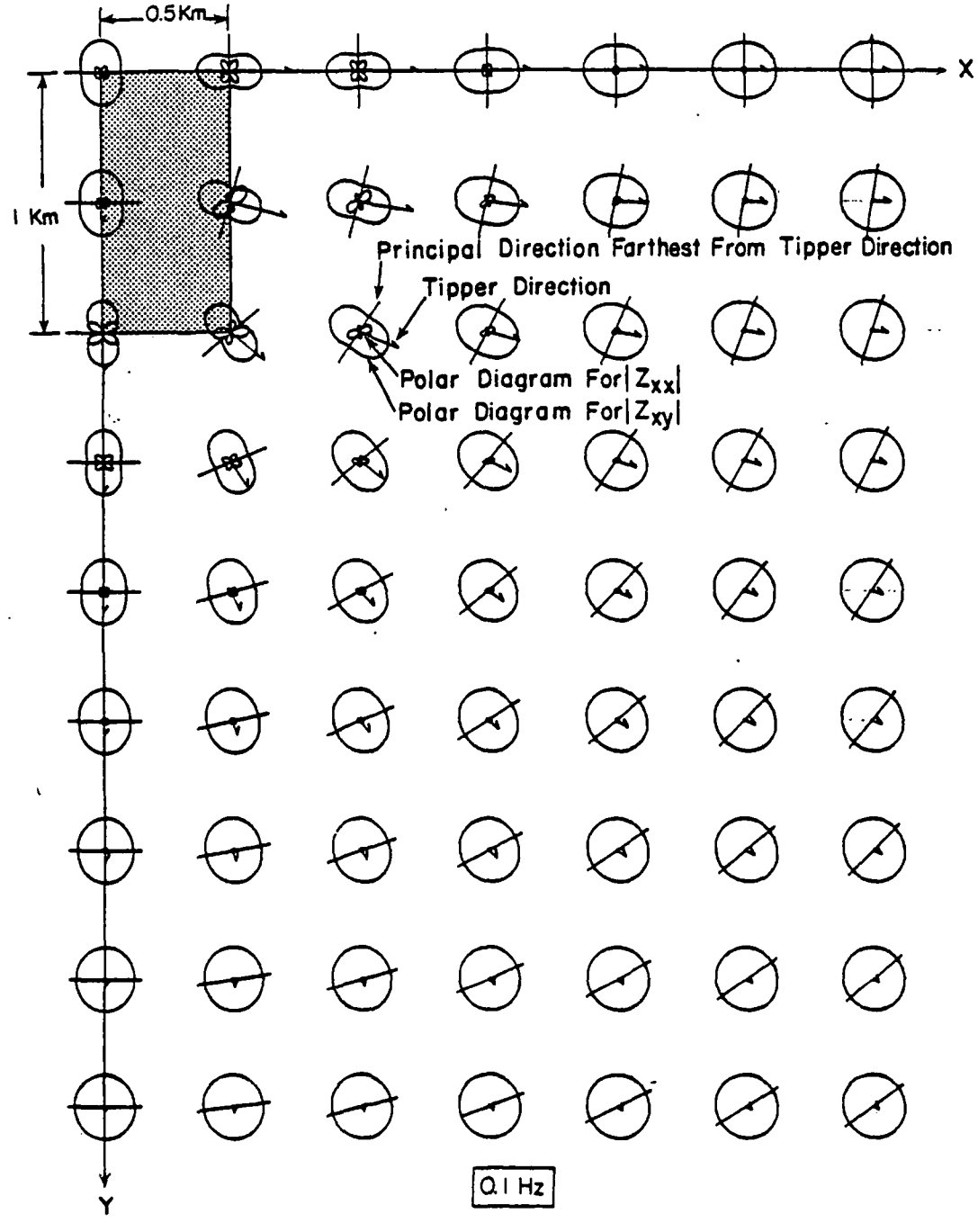
0.5Km
1 Km
X
Y
Principal Direction Farthest From Tipper Direction
Tipper Direction
Polar Diagram For $|Z_{xx}|$
Polar Diagram For $|Z_{xy}|$
0.1 Hz

Figure 15

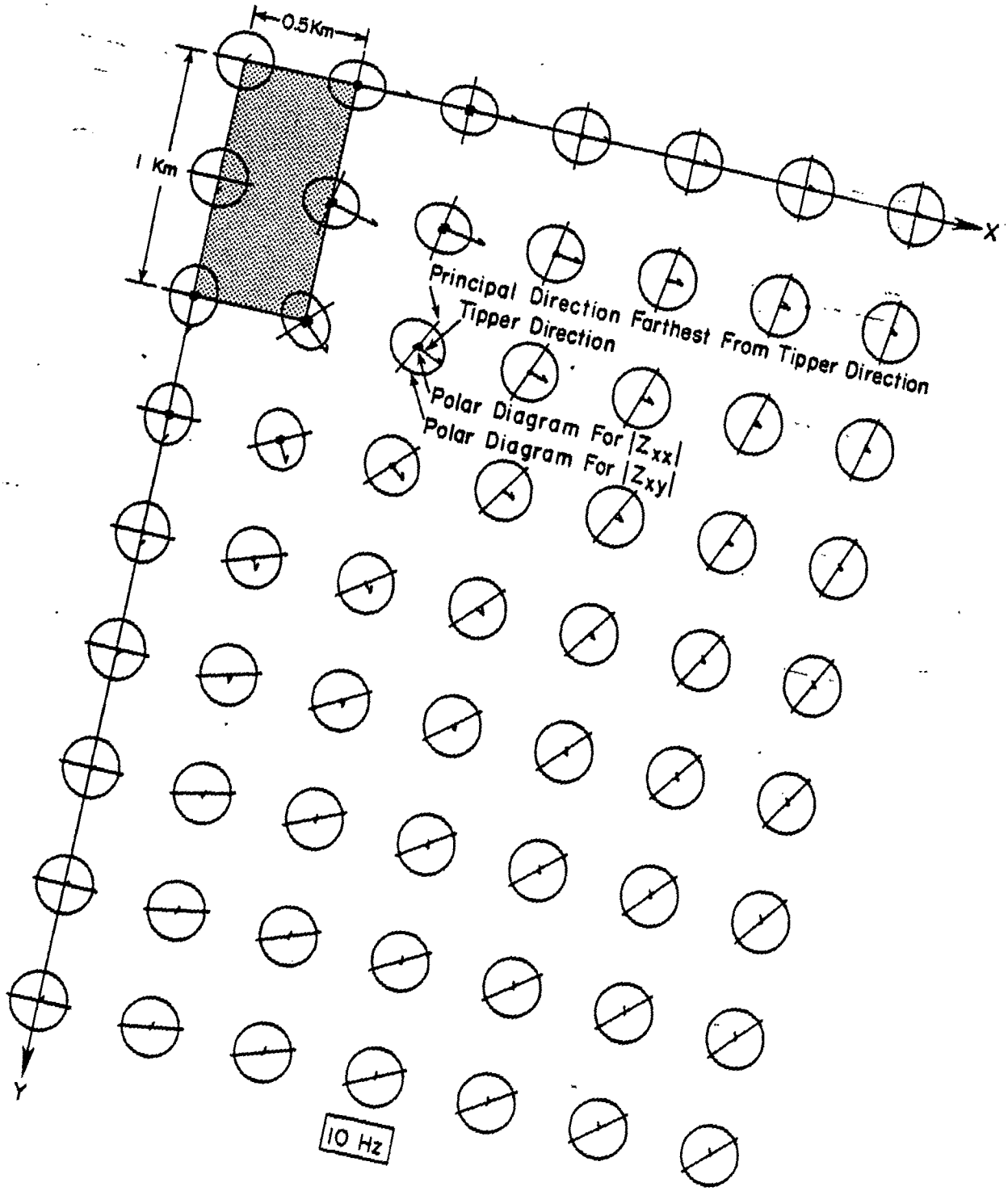
0.5Km
1 Km
X
Y
Principal Direction Farthest From Tipper Direction
Tipper Direction
Polar Diagram For |Zxx|
Polar Diagram For |Zxy|
10 Hz

Figure 16

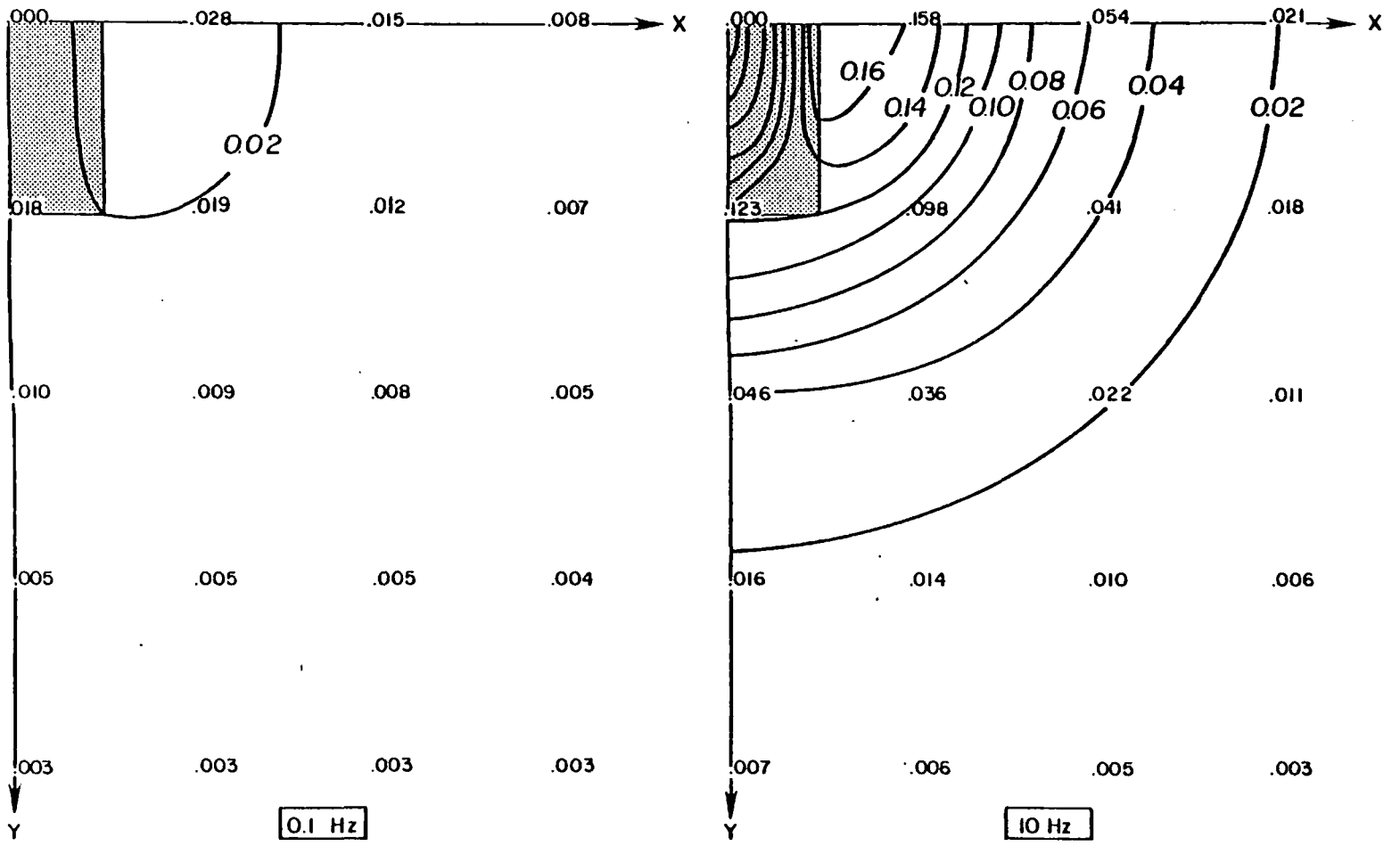
.000
.028
.015
.008
X
0.02
.018
.019
.012
.007
.010
.009
.008
.005
.005
.005
.005
.004
.003
.003
.003
.003
Y
0.1 Hz
.000
.158
.054
.021
X
0.16
0.14
0.12
0.10
0.08
0.06
0.04
0.02
.123
.098
.041
.018
.046
.036
.022
.011
.016
.014
.010
.006
.007
.006
.005
.003
Y
10 Hz

Figure 17

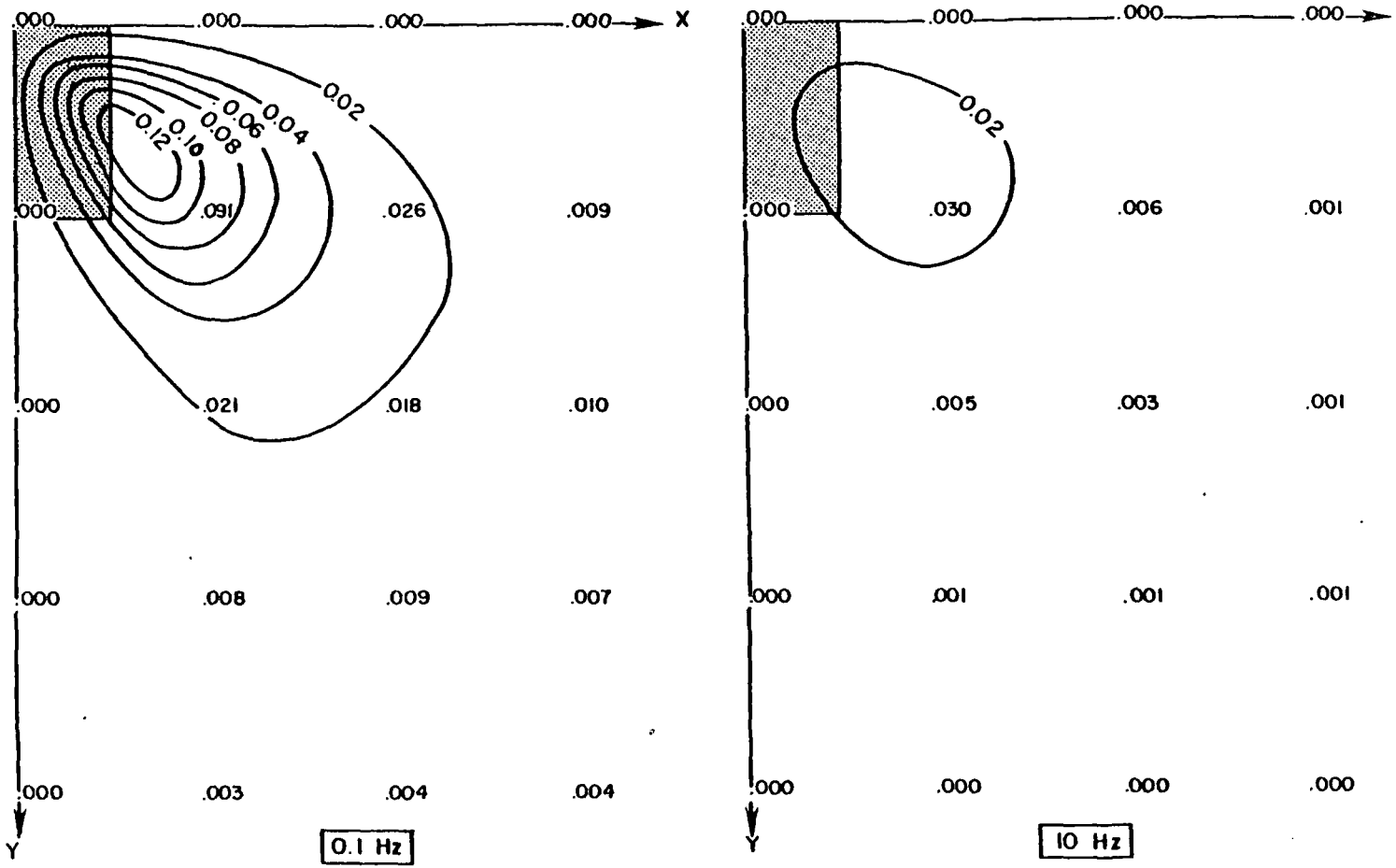
.000
.000
.000
.000
X
0.02
0.04
0.06
0.08
0.10
0.12
.091
.026
.009
.000
.021
.018
.010
.000
.008
.009
.007
.000
.003
.004
.004
Y
0.1 Hz
.000
.000
.000
.000
X
0.02
.030
.006
.001
.000
.005
.003
.001
.000
.001
.001
.001
.000
.000
.000
.000
Y
10 Hz

Figure 18

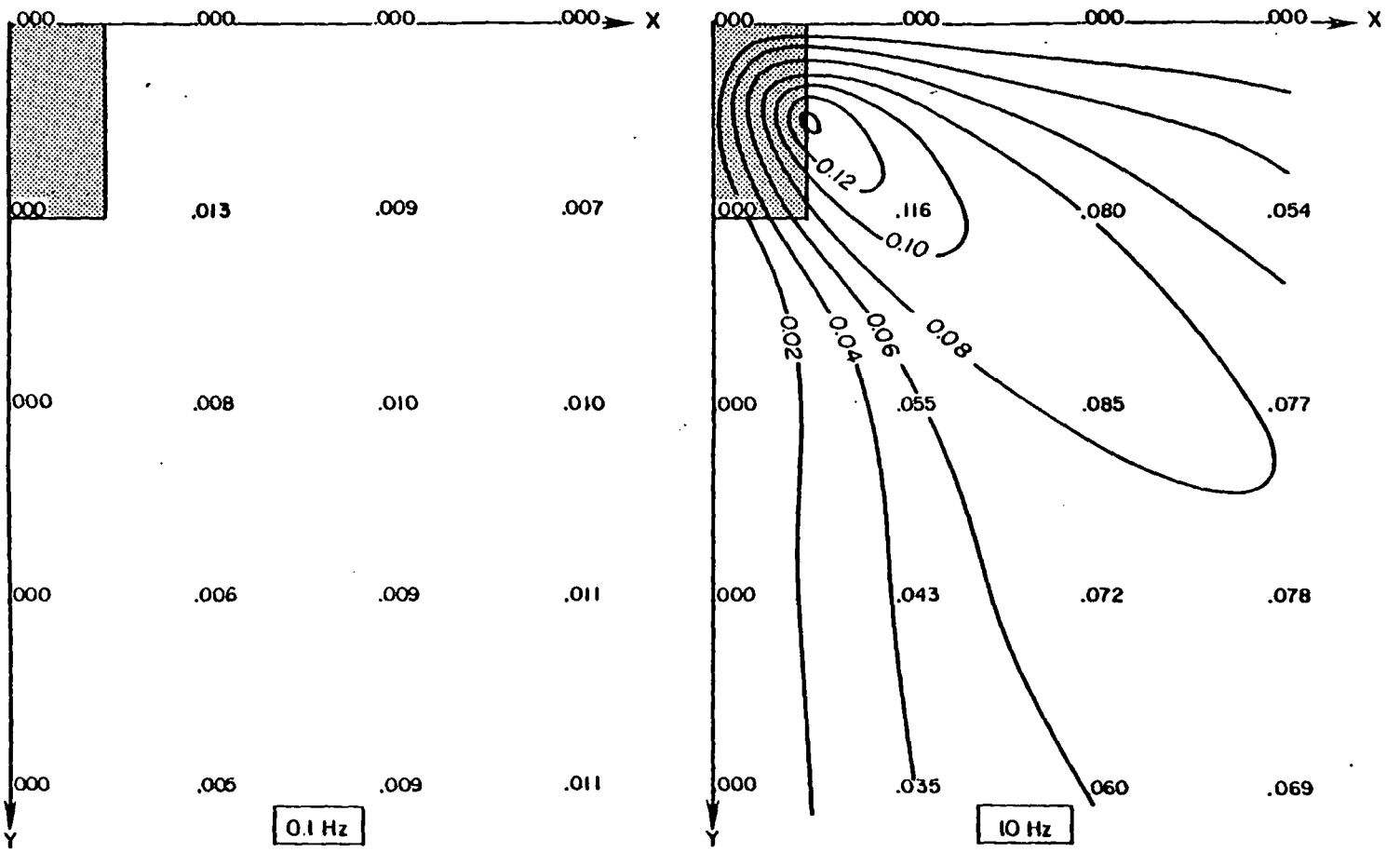
.000
.000
.000
.000
X
.000
.013
.009
.007
.000
.008
.010
.010
.000
.006
.009
.011
.000
.006
.009
.011
Y
0.1 Hz
.000
.000
.000
.000
X
0.12
0.10
0.08
0.06
0.04
0.02
.000
.116
.080
.054
.000
.055
.085
.077
.000
.043
.072
.078
.000
.035
.060
.069
Y
10 Hz

Figure 19